The Astrophysical Journal, 580:285–304, 2002 November 20

THE STRUCTURE AND EVOLUTION OF THE LAGOON NEBULA. I. SUBMILLIMETER CONTINUUM AND CO LINE MAPPING

N. F. H. Tothill,[1,2,3] Glenn J. White,[2,4] H. E. Matthews,[5,6] W. H. McCutcheon,[7]
M. J. McCaughrean,[8] and M. A. Kenworthy[9,10]
Received 2002 January 3; accepted 2002 July 22

ABSTRACT

We present submillimeter- and millimeter-wave maps tracing the molecular gas and dust around the edge of the H II region M8. The molecular material is clumped into cores on the scale of the beam (about 0.1 pc) whose temperatures can be estimated from CO observations. The masses of the clumps, estimated from their continuum fluxes, are consistent with a power-law mass function with index -1.7 ± 0.6, which agrees with determinations for other molecular clouds at similar resolutions, using molecular lines as tracers. The submillimeter clumps are sited at the interface between the H II region and the background molecular cloud, where they are exposed to the ultraviolet flux of OB stars. The physical parameters of the clumps are compared to published models of molecular clouds undergoing photoevaporation, suggesting that the pressure of the ionized gas exceeds the internal pressure of the clumps and, therefore, that a shock front will be driven into the clumps. The clumps themselves currently appear to be gravitationally unbound, but the compression may be sufficient to induce collapse.

Subject headings: H II regions — ISM: individual (M8) — ISM: structure — stars: formation — submillimeter

1. INTRODUCTION

The Lagoon Nebula, M8 (Messier 1781), lies in the Sagittarius-Carina arm of our galaxy, close to the Sgr 1A subgroup of the OB association Sgr OB1; this subgroup is about 20×10 pc in diameter, elongated along the Galactic plane (Melnik & Efremov 1995). M8 lies close to a number of H II regions (such as M20, the Trifid), and to the supernova remnant W28. These signposts of high-mass star formation are separated by about 30 pc (e.g., Lightfoot et al. 1984), comparable to the separation of subgroups in Sgr OB1 and to the separation of the Orion A and B clouds (e.g., Wall et al. 1996). For the purposes of this work, the distance to the complex is taken to be 1.7 kpc; an uncertainty of perhaps 0.2 kpc seems reasonable (e.g., van den Ancker et al. 1997; Georgelin & Georgelin 1970a; van Altena & Jones 1972; Humphreys 1978).

Elmegreen et al. (2000) suggest a general hierarchical structure for high-mass star formation: at the largest scale are spiral arms, consisting of giant star-forming condensations (~600 pc in size), separated by 1–2 kpc. These condensations contain several OB associations that may be divided into subgroups (10–20 pc across), separated by tens of parsecs. The hierarchical structure continues down to individual embedded clusters, with sizes of order 0.1 pc. Individual giant molecular clouds have diameters of about 50 pc (Blitz 1993), commensurate with OB associations, and contain clumpy structure on all scales. Williams, Blitz, & McKee (2000) call these substructures clumps and use the term "core" to refer to the cells of gas that form individual stars or stellar systems. On the other hand, Motte, André, & Neri (1998) use "core" to denote ~0.1 pc structures in the ρ Ophiuchi cloud, containing smaller scale condensations ("clumps"), likely to form individual stars.

The structure of a molecular cloud can be characterized as an ensemble of clumps, with a mass spectrum given by $dN/dm \propto m^{-\alpha}$; this mass spectrum has been studied over a variety of scales in different molecular line tracers (Blitz 1993). Molecular line studies with beam sizes $\gtrsim 0.1$ pc find $\alpha \approx 1.5$ within the errors (Loren 1989; Blitz 1993; Nozawa et al. 1991; Carr 1987; Stutzki & Güsten 1990; Lada, Bally, & Stark 1991; Williams & Blitz 1993; Williams, de Geus, & Blitz 1994; Williams, Blitz, & Stark 1995), over a range of about a decade in beam size and about three decades in mass (a few to a few thousand $M_\odot$). Studies with resolution 0.1–0.2 pc derive exponents of 1.6–1.7, while those with resolution $\gtrsim 0.5$ pc tend to find values of 1.3–1.4. More recent studies have used continuum mapping to trace structure with high spatial resolution ($\lesssim 0.03$ pc), giving steeper power laws: Motte et al. (1998) found $\alpha \sim 2.5$ in small protostellar cores in ρ Oph, flattening to 1.5 at low masses ($\leq 0.5\ M_\odot$); a similar spectrum was found by Johnstone et al. (2000). Testi & Sargent (1998) also found a steep mass spectrum ($\alpha \sim 2.1$) in the Serpens cloud core, and Motte et al. (2001) fitted a Salpeter law ($\alpha = 2.35$) to data from Orion B. These studies involve some form of spatial filtering: Testi & Sargent (1998) used aperture synthesis to make their map, which gives good signal-to-noise ratio (S/N) up

[1] Department of Astronomy and Physics, Saint Mary's University, Halifax, NS B3H 3C3, Canada.
[2] Department of Physics, Queen Mary and Westfield College, University of London, Mile End Road, London E1 4NS, UK.
[3] nfht@ap.stmarys.ca.
[4] School of Physical Sciences, University of Kent at Canterbury, Canterbury, Kent CT2 7NZ, UK.
[5] Joint Astronomy Centre, 660 North A'ohōkū Place, Hilo, HI 96720-6030.
[6] National Research Council of Canada, Herzberg Institute of Astrophysics, 5071 West Saanich Road, Victoria, BC V9E 2E7, Canada.
[7] Department of Physics and Astronomy, University of British Columbia, 6224 Agricultural Road, Vancouver, BC V6T 1Z1, Canada.
[8] Astrophysikalisches Institut Potsdam, An der Sternwarte 16, 14482 Potsdam, Germany.
[9] Steward Observatory, University of Arizona, 933 North Cherry Avenue, Tucson, AZ 85721.
[10] Department of Physics, University of Cincinnati, Cincinnati, OH 45221-0011.

to about 30″, i.e., ~6 beamwidths. Motte et al. (1998) used wavelet analysis on their maps to select structures: their value of $\alpha = 2.5$ was derived by removing structures on scales greater than 1′ (i.e., about 5 beamwidths); with the larger structures included, the exponent reverted to 1.5. This neat division of mass spectra by spatial resolution is, however, inconsistent with the results of Heithausen et al. (1998), who found $\alpha = 1.8$ over five decades in mass, down to a spatial resolution of ~0.02 pc, using ^{12}CO maps. Motte et al. (2001) suggest that this is because the ^{12}CO lines are largely tracing low-density unbound material, governed by turbulence in the interstellar medium, while the continuum maps show dense bound clumps in which self-gravitation is dominant.

Mapping the relatively distant star-forming region M8 allows us to measure the mass spectrum on large scales, using continuum emission as a tracer; this is complementary to the recent high-resolution continuum studies and, indeed, to large-scale molecular line work. The intention of this paper is to use continuum and CO line maps of the molecular gas around M8 to measure a clump mass spectrum, to characterize the physical conditions of these clumps, and to study their likely future evolution in this highly energetic region.

2. OBSERVATIONS, DATA REDUCTION, AND CALIBRATION

2.1. *Submillimeter Continuum Observations*

M8 was observed with the Submillimeter Common-User Bolometer Array (SCUBA; Holland et al. 1999) on the James Clerk Maxwell Telescope (JCMT) for a total of 16 hours over five nights in 1998 April, in good weather conditions ($0.04 \leq \tau_{225} \leq 0.08$), at wavelengths of 450 and 850 μm. The observations used scan-mapping mode, in which the bolometer arrays are scanned over the sky at specific position angles (in Nasmyth coordinates) in order to generate fully sampled maps of a strip of sky; a number of these strips make up a map. Each field was mapped six times, each time with a different chop throw: 20″, 30″, and 65″ in both right ascension and declination. This combination gives good sensitivity to emission with spatial wavelength greater than 5″. The scan maps of M8 were made up of two overlapping fields, eastern and western, each ~10′ square.

The data were reduced with the standard software (SURF; Jenness & Lightfoot 1997); this uses the deconvolution technique suggested by Emerson (1995). The reduction process consisted of flat-fielding, despiking and editing the data to remove excessive noise, extinction correction by linear interpolation between known values of atmospheric extinction (measured every hour or so by telescope skydip), removal of additive offsets between individual bolometer scans by subtracting the median value of the scan, and correction for pointing drifts by linear interpolation between successive pointing checks.

Scan maps of Uranus (using the same mapping protocol as the M8 maps) were used to flux-calibrate the data. The accuracy of the flux calibration is subject to uncertainties in the assumed fluxes of planetary calibrators, the gain of the system, and the opacity of the atmosphere. Adding the various errors in quadrature, the estimated calibration errors are between 8% and 11% for 450 μm data (depending on the assumptions employed) and 6% for 850 μm data (dominated by the uncertainty in the flux of Mars).

The calibrated scans were then rebinned into a series of double-beam maps, each corresponding to a given chop throw. These double-beam maps were then deconvolved by Fourier transforming them, co-adding them in Fourier space, and dividing by the spatial-frequency response of the combination of six chop throws (equivalent to deconvolving the double-beam pattern), then back-transforming into a final single-beam map, calibrated in Jy beam^{-1} (Figs. 1 and 2).

2.2. *Millimeter Continuum Observations*

A 1.3 mm wavelength map was obtained over 20 hours of telescope time in 1998 March at the 30 m Millimeter-wave

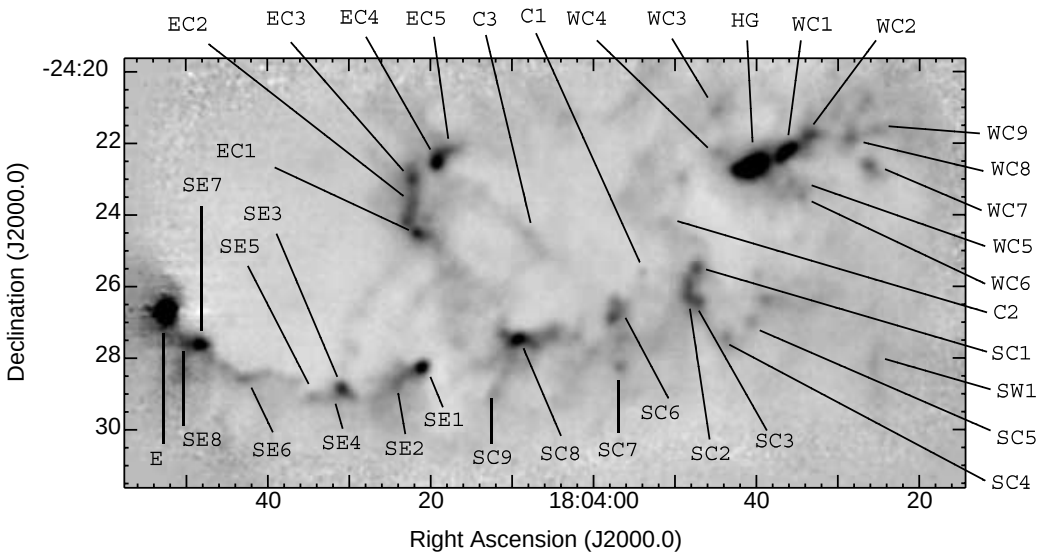

FIG. 1.—Single-beam map of the Lagoon Nebula at 850 μm. The intensity cuts are –0.4 Jy beam^{-1} (*white*) and 1.2 Jy beam^{-1} (*black*). The annotations give the names of the clumps.

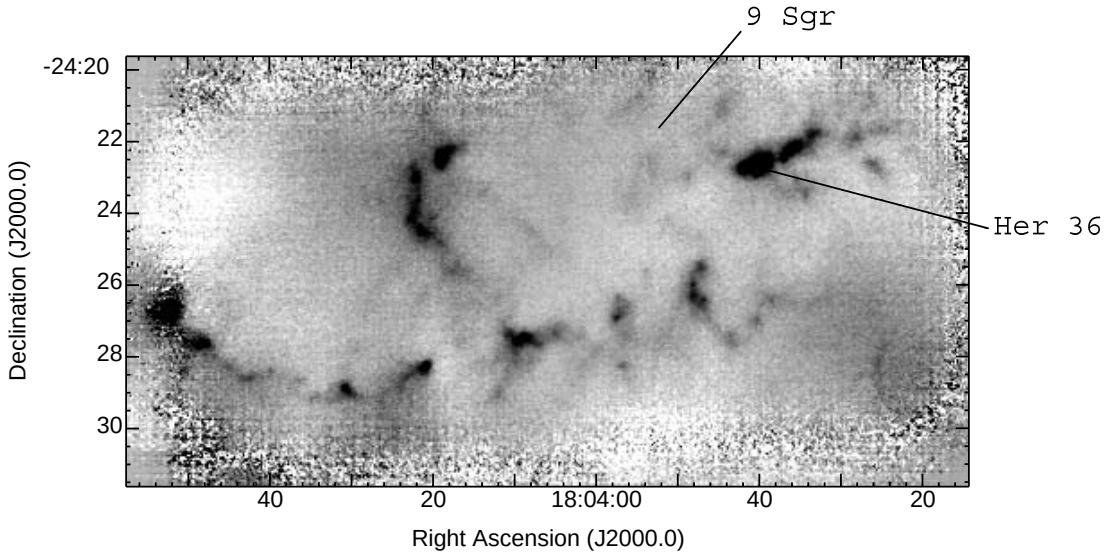

FIG. 2.—Single-beam map of the Lagoon Nebula at 450 μm. The intensity cuts are –1.4 Jy beam^{-1} (*white*) and 3.5 Jy beam^{-1} (*black*). The annotations show the locations of the stars powering the various H II regions; HD 165052 is outside the map, to the east.

Radio Telescope (MRT) operated by IRAM at Pico Veleta, using the MPIfR 37 channel bolometer array (Kreysa et al. 1998). The zenith opacity at 1.3 mm varied from 0.13 to 0.45 (corresponding to 1.5–6 mm precipitable water vapor). The mapping parameters were set to suit large-area mapping—a scanning speed of $6'' \ s^{-1}$ and pixel size of $5'' \times 5''$—to allow individual maps ($\sim 8' \times \sim 4'$) to be made in about an hour, in turn allowing frequent calibration. The mapping was carried out in horizontal coordinates, chopping along the scan direction at constant elevation with a $46''$ throw.

The data were reduced with the NIC software package (Broguière, Neri, & Sievers 1998),[11] which uses a mapping technique slightly different to that discussed above: while SCUBA is treated as a camera that builds up a fully sampled map of the sky, the MPIfR array is considered to be a set of single-channel bolometers, each of which maps the sky independently. The data were flat-fielded, i.e., corrected for the known gain of the channel relative to the reference channel, and converted to Jy beam^{-1}. Bad data were edited out, and a baseline (usually second order) was subtracted. Then the data for each bolometer were converted into a double-beam map of the sky in horizontal coordinates, and the double-beam response was deconvolved using the EKH algorithm (Emerson, Klein, & Haslam 1979). Finally, all 37 single-beam maps were regridded and co-added into a single map in equatorial coordinates.

This basic procedure was used iteratively to reduce sky noise (Broguière et al. 1998): the single-beam map was used to distinguish the parts of the map containing astronomical emission. The sky noise should be correlated across the bolometers, so those parts of the map considered to be free of astronomical emission were used to estimate the sky emission and hence remove that emission from all the channels. The noise-reduced data was then processed into a new single-beam map. Iterating this process led to a greatly improved map (Fig. 3).

[11] Available from http://www.iram.es.

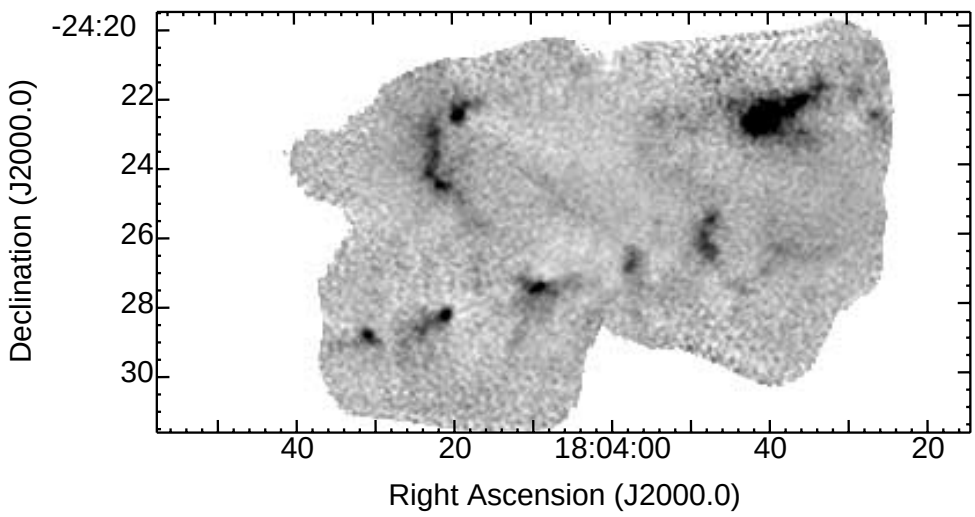

FIG. 3.—Single-beam map of the Lagoon Nebula at 1.3 mm. The intensity cuts are −80 mJy beam^{-1} (*white*) and 200 mJy beam^{-1} (*black*).

As with the SCUBA observations, the flux calibration of the maps was referred to measurements of Uranus, taken about once a night, corrected for beam coupling and for variations in the effective frequency of observation (due to atmospheric opacity). Uncertainties in the calibration arise from integration time smearing of the calibrator, scatter in the gain calibration measurements, uncertainties in the flux models of the calibrators (as above), errors in the atmospheric opacity, and gain variations due to elevation (Greve, Neri, & Sievers 1998). The overall flux uncertainty is estimated to be 15%.

2.3. CO *Line Observations*

Maps of the $J = 3$–2 emission from ^{12}CO, ^{13}CO, and C^{18}O were obtained in 1996 April at the JCMT, using on-the-fly (OTF) mapping and the facility autocorrelation spectrometer, with a resolution of 0.17 km s^{-1}. The map cell size was $10'' \times 10''$, somewhat undersampling the $\sim 15''$ beam, and the intensities were calibrated onto the T_R^* scale, using $\eta_{\rm fss} = 0.8$.

Further OTF maps of the southeastern parts of M8 were obtained in the $J = 2$–1 transitions of ^{12}CO, ^{13}CO, and C^{18}O, at the 10 m Heinrich Hertz Telescope (HHT) over three nights in 2000 May, covering the southeastern parts of the region, which were not mapped at the JCMT. The maps were sampled at intervals of $5''$ in right ascension (the scan direction) and $10''$ in declination, fully sampling the $\sim 30''$ beam. Additional pointed observations toward clump centers were obtained in C^{18}O. Facility instrumentation was used: the 230 GHz receiver fed a filter bank spectrometer with a resolution of 0.34 km s^{-1}, and data reduction was carried out with GILDAS software, removing fourth-order baselines and treating the spectra as random spatial samples due to the irregularity of OTF mapping. A few spectra were dropped from the ^{12}CO map because of instrumental problems, and one of the mapping scans had a consistently "hot" velocity channel, which was interpolated from its two neighbors. The HHT does not have continuous calibration: a cold load was measured at the start of each night, and subsequent calibrations, using hot and sky loads only, were carried out between scans.

The off-source reference position at the HHT was $2700''$ east of the map origin; the ^{12}CO emission toward this position was estimated by a series of position-switched integrations with switch throws of $(0'', -1000'')$, $(0'', -2700'')$, and $(2700'', 0'')$ in equatorial coordinates. The weighted mean of these observations was taken to be the ^{12}CO spectrum of the map reference position, with a peak T_A^* of 7 K, line width of 1.4 km s^{-1} and a slight red wing. (This is, of course, a lower limit to the emission, due to the effect of position switching.) This was added back into the map spectra, which were divided by $\eta_{\rm mb}$ $(= 0.8)$ to give values of $T_{\rm mb}$. Although this is not consistent with the use of T_R^* for the JCMT data, the HHT data had twice the beamwidth, so the use of $T_{\rm mb}$ is probably more accurate for the 2–1 transitions.

3. DATA ANALYSIS: FROM FLUX TO MASS

3.1. *Characterizing the Beams*

The simplest approximation to the telescope beam is a Gaussian. Although this is generally a good approximation to the main lobe of the telescope power pattern, it does not include the contribution of the error lobes. The beam integral of a Gaussian beam (the "Gaussian beam integral") within a circular aperture co-centered with the beam can be calculated analytically, but the true beam integral over a given aperture must be measured from a beam map. Maps of the 450 and 850 μm beams were produced from observations of Uranus: the error beam has power levels about 5% of the peak power at 850 μm and about 10% at 450 μm. A scan map of Uranus (taken 2 weeks before the M8 observations) was used to characterize the MRT beam. This is defined in horizontal coordinates, but the source map is produced by the co-addition of multiple maps with different scan directions due to source rotation. Thus the MRT beam map is not strictly the same as the PSF of the system.

Gaussian profiles fitted to the planet maps overestimate the measured telescope HPBW (even taking into account the size of Uranus in the beam), and the measured peak intensity underestimates the predicted flux of Uranus in the telescope beam. Both effects are much more severe at 450 μm than at 850 μm, and are presumably caused by the error beam, which is far more prominent at 450 μm. Figure 4 shows the beam integrals at all three wavelengths, measured in circular apertures of varying radius, together with Gaussian beam integrals in the same apertures, assuming the Gaussian FWHM fitted to the planet maps. The measured beam integrals in Figure 4 are consistent with previous characterizations of the JCMT beam (Richer 1992; Hobson et al. 1993; Shirley et al. 2000). The 450 μm beam integral is reduced at certain radii, due to regions of negative power.

The maps were smoothed so as to give resolution equal to that of the broadest main beam, in this case, the $15\farcs2$ 850 μm beam of the JCMT. This procedure took no account of the error beam but merely attempted to match the main beams at the various wave bands, assuming Gaussian beam profiles. The smoothed Gaussian FWHMs of all the beams agree to about 10%.

3.2. *Measuring the Clumps*

The continuum maps of M8 (Figs. 1, 2, and 3) show a large number of extended clumps superposed on more diffuse emission, a structure that makes aperture photometry impractical, so Gaussian profiles were fitted to the clumps. This implicitly assumes that the intensity distribution of the clump can be well represented by a Gaussian profile. Theoretically, star-forming cores are expected to have a power-law density profiles with an index between $-3/2$ and -2 (e.g., Shu 1977); this translates approximately into a power-law submillimeter intensity profile (Adams 1991). Studies of radial intensity profiles in nearby low-mass star-forming regions tend to bear out the notion of power-law brightness distributions for Class 0/I sources but show much flatter profiles for prestellar condensations (e.g., Motte & André 2001; Shirley et al. 2000; Ward-Thompson, Motte, & André 1999); the likely intensity structure of submillimeter sources in high-mass star-forming regions is not well known. Since Stutzki & Güsten (1990) pointed out that fitted Gaussians still give useful estimates of the parameters (such as size) of non-Gaussian structures, and Ladd et al. (1991) found that power-law sources can be fitted fairly well by Gaussian profiles, the assumption of Gaussian structure does not appear to be particularly harmful.

Profile fitting was carried out on the smoothed maps, so Gaussians at different wavelengths should be fitted to

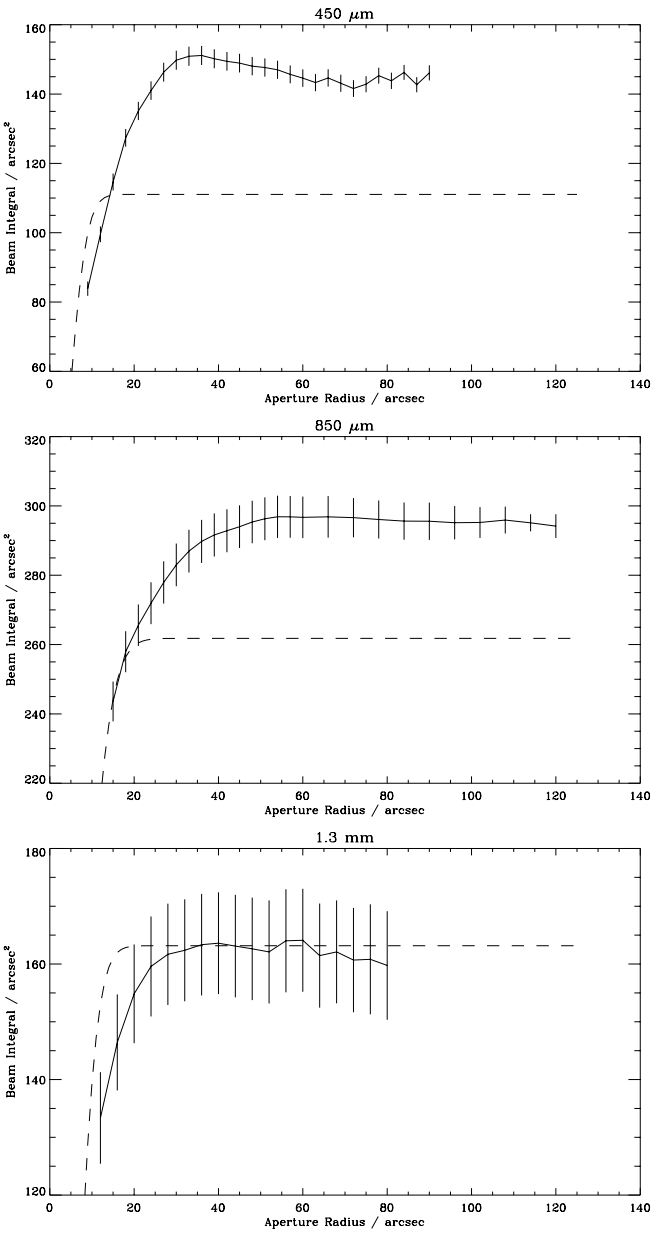

FIG. 4.—Measured and calculated beam integrals for all three wave bands. The solid line is the measured beam integral; the vertical lines are 1 σ error bars in the photometry. The broken line is the calculated Gaussian beam integral.

similar structure in the map; the procedure included the subtraction of a local background level and is discussed in detail in the Appendix. The Gaussian-fitting procedure was carried out independently on the three maps, producing three lists of fitted Gaussian sources, with the following parameters: the offset from the map reference position, the geometric-mean FWHM of the source, and the integrated flux of the Gaussian. Lists of all detected clumps are available elsewhere (Tothill 1999). It is difficult to define a detection limit: the brightest clumps are surrounded by imaging artifacts at a level of order 10% of the clump peak, so it is unlikely that clumps fainter than this can be reliably detected, giving limits of about 0.4, 1, and 0.08 Jy beam^{-1} at 850 μm, 450 μm, and 1.3 mm, respectively. However, in regions without bright emission, clumps with peak brightnesses as low as about 0.1, 0.3 and 0.02 Jy beam^{-1} (at 850 μm, 450 μm, and 1.3 mm) have been successfully fitted with Gaussians.

For each wavelength, a sample of sources was selected, first by removing Gaussian fits with a fractional error greater than 20% in either FWHM or amplitude: 10 Gaussians out of 67 at 450 μm, two out of 62 at 850 μm, and three out of 37 at 1.3 mm. Clump detections at only one wavelength were rejected, even if the single detection was at high S/N. Cross-referencing by position gave two subsamples of clumps: 17 clumps detected at all wavelengths (the "3-d" sample) and 20 detected at both 450 μm and 850 μm (the "2-d" sample). The whole mapped field is divided into six notional sections: SE, SW, EC, SC, WC, and C; clumps in the two subsamples are assigned numbers within these regions. The two brightest sources in the map, the Hourglass Nebula (M8HG) and M8E, are designated separately inside M8WC and M8SE.

The distributions of 850 μm fluxes in the two samples were compared, using a Kolmogorov-Smirnov (K-S) test (e.g., Press et al. 1986, § 13.5), a robust method of determining whether or not two distributions are consistent with one another. The K-S test did not exclude the possibility of 3-d and 2-d samples being consistent but did suggest that the 2-d sample tends to consist of fainter clumps than the 3-d sample. K-S tests were also used to check whether the flux distribution of the selected sample was different from that of all Gaussian-fitted fluxes in a given wave band: there is no evidence that the requirement of simultaneous detection has significantly biased the sample toward either high- or low-flux sources.

Since the maps were smoothed to the same resolution, it might be expected that the fitted Gaussians in different maps would have the same size. In fact, a comparison of the fitted areas shows that there is a large scatter in geometric-mean FWHM. If this scatter is interpreted as being due to errors in the Gaussian fitting, it will affect the accuracy of the flux measurements (derived by integrating the Gaussians). The mean-square fractional scatters in fitted area were estimated for all wave bands and found to be larger than expected from the uncertainties estimated by the fitting routine. The excess error could be caused by the routine attempting to fit slightly different map structure to the same Gaussian at different wavelengths or by the attempt to fit a Gaussian profile to a non-Gaussian structure. It was treated as an additional independent error on all flux measurements of 35%, 9%, and 27% at 450 μm, 850 μm, and 1.3 mm.

Tables 1 and 2 list the ellipticities, geometric-mean FWHM and fluxes of the clumps in the 3-d and 2-d samples, together with their estimated errors. Table 1 gives the 850 μm data on the clumps, together with their offsets from the reference position in arcseconds and the physical size of the FWHM in parsecs, derived from the 850 μm fits. Table 2 gives the ellipticities, geometric-mean FWHM, and fluxes at 450 μm and 1.3 mm.

3.3. CO *Line Data*

CO spectra toward the clumps were extracted from the maps and analyzed to complement the continuum measurements. From the 3–2 maps, the closest sampled spectrum was used: the maps were taken on a 10″ grid, so each spectrum was $\lesssim 7''$ away. The spectral lines were characterized by fitting Gaussian profiles, giving the amplitude (peak

TABLE 1
850 μm Sources

Clump	$\Delta\alpha$ (arcsec)	$\Delta\delta$ (arcsec)	e_{850}	θ_{850} (arcsec)	S_{850} (Jy)	D_{850} (pc)
			3-d Sample			
HG	−183	101	0.15 ± 0.01	19.5 ± 0.6	5.88 ± 0.78	0.16 ± 0.02
WC1	−239	127	0.0074 ± 0.005	21.6 ± 2.2	2.27 ± 0.60	0.18 ± 0.03
WC2	−278	152	0.014 ± 0.03	30.6 ± 2.0	2.69 ± 0.51	0.25 ± 0.03
EC1.....	376	−9	$(7.3 \pm 4) \times 10^{-6}$	23.6 ± 2.3	2.00 ± 0.52	0.19 ± 0.03
EC3.....	386	81	$(1.8 \pm 4) \times 10^{-6}$	27.8 ± 1.8	2.21 ± 0.44	0.23 ± 0.03
EC4.....	344	11	0.0091 ± 0.003	24.9 ± 1.1	3.53 ± 0.51	0.21 ± 0.02
SE1	375	−239	0.37 ± 0.01	28.5 ± 0.7	5.10 ± 0.61	0.23 ± 0.02
SE2	413	−262	0.012 ± 0.04	28.6 ± 2.1	1.38 ± 0.30	0.24 ± 0.02
SE3	503	−276	$(9.5 \pm 3) \times 10^{-5}$	31.7 ± 1.0	4.02 ± 0.52	0.26 ± 0.03
SC1	−90	−71	0.019 ± 0.02	21.0 ± 2.3	0.96 ± 0.30	0.17 ± 0.03
SC2.....	−82	−118	0.032 ± 0.06	30.8 ± 1.5	2.34 ± 0.35	0.25 ± 0.03
SC4.....	−140	−188	$(53 \pm 9) \times 10^{-5}$	30.2 ± 1.5	1.26 ± 0.19	0.25 ± 0.03
SC5.....	−184	−158	0.0028 ± 0.001	20.9 ± 1.2	0.44 ± 0.08	0.17 ± 0.02
SC6.....	47	−123	0.0095 ± 0.03	18.4 ± 0.9	0.40 ± 0.06	0.15 ± 0.02
SC7.....	38	−233	$(22 \pm 9) \times 10^{-5}$	21.0 ± 0.6	0.67 ± 0.08	0.17 ± 0.02
SC8.....	209	−191	0.011 ± 0.003	34.0 ± 3.3	6.70 ± 1.64	0.28 ± 0.04
C1	0	−80	$(7.2 \pm 2) \times 10^{-7}$	22.2 ± 1.4	0.42 ± 0.08	0.18 ± 0.02
			2-d Sample			
WC3	−125	197	0.0093 ± 0.01	19.1 ± 1.3	0.36 ± 0.07	0.16 ± 0.02
WC4	−130	124	$(1.4 \pm 3) \times 10^{-5}$	31.0 ± 0.8	1.48 ± 0.19	0.26 ± 0.03
WC5	−248	71	0.056 ± 0.04	23.6 ± 2.6	0.48 ± 0.14	0.19 ± 0.03
WC6	−266	56	0.015 ± 0.02	28.3 ± 2.3	1.37 ± 0.32	0.23 ± 0.03
WC7	−381	102	$(5.0 \pm 10) \times 10^{-6}$	27.1 ± 1.1	1.75 ± 0.24	0.22 ± 0.02
WC8	−348	152	0.012 ± 0.003	29.0 ± 0.9	1.50 ± 0.19	0.24 ± 0.03
WC9	−392	163	0.0078 ± 0.007	22.4 ± 1.5	0.52 ± 0.10	0.18 ± 0.02
SW1	−388	−229	0.044 ± 0.04	29.0 ± 3.2	0.74 ± 0.22	0.24 ± 0.04
EC2.....	388	53	0.013 ± 0.01	28.9 ± 1.0	1.41 ± 0.18	0.24 ± 0.03
EC5.....	327	133	0.49 ± 0.03	28.5 ± 1.3	1.76 ± 0.26	0.23 ± 0.03
E	797	−140	0.0010 ± 0.0003	24.7 ± 0.4	8.75 ± 1.01	0.20 ± 0.02
SE4	529	−291	0.011 ± 0.002	15.8 ± 1.6	0.17 ± 0.05	0.13 ± 0.02
SE5	550	−288	0.012 ± 0.01	24.5 ± 0.8	0.88 ± 0.12	0.20 ± 0.02
SE6	668	−256	0.017 ± 0.006	29.1 ± 1.2	1.36 ± 0.20	0.24 ± 0.03
SE7	742	−197	0.26 ± 0.02	20.9 ± 0.9	2.38 ± 0.35	0.17 ± 0.02
SE8	770	−193	$(3.4 \pm 2) \times 10^{-6}$	23.5 ± 2.0	1.03 ± 0.24	0.19 ± 0.02
SC3.....	−95	−133	0.36 ± 0.03	23.3 ± 1.5	0.71 ± 0.13	0.19 ± 0.02
SC9.....	246	−280	0.46 ± 0.02	38.3 ± 2.4	2.82 ± 0.52	0.32 ± 0.04
C2	−39	6	0.014 ± 0.06	19.1 ± 3.0	0.18 ± 0.07	0.16 ± 0.03
C3	192	−11	$(5.9 \pm 2) \times 10^{-5}$	17.5 ± 1.7	0.23 ± 0.06	0.14 ± 0.02

Note.—Parameters for the 3-d and 2-d samples (the upper and lower halves of the table, respectively): ellipticity (e_{850}), geometric-mean FWHM (θ_{850}), and flux (S_{850}) are given, along with the position of the clump and its physical size, both derived from 850 μm data.

temperature), the FWHM Δv, and the central line velocity v. Asymmetric or double-peaked lines were fitted by the sum of two Gaussians, and one of the components was taken to be associated with the continuum clump. This was usually done by examination of ^{12}CO and ^{13}CO spectra—the component that was proportionately stronger in ^{13}CO was selected. For some clumps, the ^{12}CO and ^{13}CO lines had very different shapes, suggesting self-absorption in the ^{12}CO line, and these spectra were not used. For the 2–1 maps covering the M8SE region, the closest ^{12}CO spectrum was extracted for each clump, while the ^{13}CO spectrum was obtained by co-adding all spectra within 5″ of the clump position to improve S/N. C^{18}O spectra used spectra within 10″ in addition to longer pointed observations. The Gaussian fit parameters for all lines are given in Tables 3 (3–2) and 4 (2–1).

Figure 5 shows the integrated intensity of ^{12}CO 3–2 and ^{12}CO 2–1 (toward M8SE) superposed on the 850 μm emission. At low levels, the agreement between the two tracers is excellent. Based on the possibility of line contamination discussed in § 3.4.2 below, the low-level emission at 850 μm may be largely composed of molecular line emission, mainly ^{12}CO. At higher intensities, the maps do not match particularly well—many of the continuum peaks are found just off ^{12}CO peaks. Similar mismatches between continuum and CO peaks have been seen even in more optically thin isotopomeric transitions by Mitchell et al. (2001). This could be explained by the ^{12}CO emission (which traces temperature) being concentrated at the edges of the clumps, while the continuum emission peaks at the center, or by the ratio of CO to dust abundances varying with position, possibly due to freezeout. However, freezeout is expected to be important

TABLE 2

450 μm AND 1.3 mm SOURCES

Clump	e_{450}	θ_{450} (arcsec)	S_{450} (Jy)	$e_{1.3}$	$\theta_{1.3}$ (arcsec)	$S_{1.3}$ (Jy)
			3-d Sample			
HG	0.12 ± 0.01	19.5 ± 0.6	36.8 ± 13.8	0.028 ± 0.03	22.0 ± 1.4	2.64 ± 0.91
WC1	0.54 ± 0.01	29.9 ± 1.0	42.6 ± 15.9	0.012 ± 0.04	20.9 ± 3.2	0.52 ± 0.24
WC2	0.0073 ± 0.002	31.5 ± 2.3	22.6 ± 9.2	0.22 ± 0.03	35.4 ± 2.8	0.93 ± 0.33
EC1.....	$(3.9 \pm 1) \times 10^{-8}$	21.8 ± 1.6	8.0 ± 3.2	0.0026 ± 0.0007	23.6 ± 2.6	0.43 ± 0.17
EC3.....	$(1.9 \pm 1) \times 10^{-6}$	26.9 ± 2.0	13.8 ± 5.6	0.00090 ± 0.02	36.8 ± 1.3	1.06 ± 0.34
EC4.....	0.28 ± 0.01	27.6 ± 0.9	29.9 ± 11.2	$(7.8 \pm 3) \times 10^{-6}$	24.2 ± 0.6	0.81 ± 0.26
SE1	0.23 ± 0.02	22.4 ± 1.6	21.4 ± 8.9	0.023 ± 0.02	25.7 ± 1.5	0.93 ± 0.31
SE2	0.015 ± 0.004	22.2 ± 0.7	3.4 ± 1.3	0.35 ± 0.03	33.0 ± 2.5	0.59 ± 0.21
SE3	0.024 ± 0.02	31.6 ± 1.4	30.4 ± 11.6	0.013 ± 0.03	26.2 ± 1.2	0.68 ± 0.22
SC1	0.21 ± 0.02	36.4 ± 1.6	32.5 ± 12.5	0.38 ± 0.03	21.7 ± 1.7	0.23 ± 0.09
SC2	0.41 ± 0.03	32.3 ± 1.9	22.8 ± 9.0	0.031 ± 0.03	38.3 ± 2.6	0.97 ± 0.33
SC4	$(8.7 \pm 1) \times 10^{-4}$	28.3 ± 1.1	7.9 ± 3.0	0.0017 ± 0.0003	28.8 ± 1.5	0.24 ± 0.08
SC5	0.0040 ± 0.002	21.9 ± 1.1	4.2 ± 1.6	0.0092 ± 0.02	25.6 ± 1.5	0.19 ± 0.06
SC6	0.023 ± 0.03	26.5 ± 1.7	8.2 ± 3.3	$(1.8 \pm 6) \times 10^{-6}$	23.9 ± 1.2	0.22 ± 0.07
SC7	0.014 ± 0.01	17.7 ± 0.6	2.6 ± 1.0	$(6.6 \pm 200) \times 10^{-6}$	17.0 ± 2.3	0.07 ± 0.03
SC8	0.40 ± 0.01	32.3 ± 2.0	46.0 ± 18.2	0.046 ± 0.05	26.8 ± 3.4	0.79 ± 0.34
C1	0.0070 ± 0.03	25.2 ± 0.8	3.5 ± 1.3	0.011 ± 0.04	15.6 ± 0.8	0.06 ± 0.02
			2-d Sample			
WC3	0.0033 ± 0.0008	31.0 ± 1.8	8.6 ± 3.3	...	...	...
WC4	0.028 ± 0.03	18.4 ± 2.7	1.9 ± 1.0	...	...	...
WC5	$(4.0 \pm 0.8) \times 10^{-6}$	26.4 ± 2.7	5.1 ± 2.3	...	...	...
WC6	0.21 ± 0.02	20.4 ± 1.2	3.4 ± 1.3	...	...	...
WC7	$(3.0 \pm 20) \times 10^{-7}$	27.0 ± 2.1	11.5 ± 4.8	...	...	...
WC8	$(1.1 \pm 10) \times 10^{-5}$	30.9 ± 1.8	14.7 ± 5.8	...	...	...
WC9	0.44 ± 0.02	27.3 ± 1.8	6.4 ± 2.6	...	...	...
SW1	$(1.8 \pm 0.9) \times 10^{-5}$	22.0 ± 1.6	3.0 ± 1.2	...	...	...
EC2.....	$(1.8 \pm 0.8) \times 10^{-5}$	37.6 ± 3.9	21.2 ± 10.0	...	...	...
EC5.....	0.29 ± 0.028	26.1 ± 1.2	10.2 ± 3.9	...	...	...
E	0.011 ± 0.007	18.9 ± 0.7	41.8 ± 15.8	...	...	...
SE4	$(9.9 \pm 1) \times 10^{-6}$	28.8 ± 1.0	7.1 ± 2.7	...	...	...
SE5	0.27 ± 0.01	27.9 ± 0.9	8.8 ± 3.3	...	...	...
SE6	0.55 ± 0.02	28.6 ± 1.5	10.0 ± 3.9	...	...	...
SE7	0.015 ± 0.03	25.1 ± 1.9	25.5 ± 10.5	...	...	...
SE8	0.26 ± 0.01	24.9 ± 1.7	10.9 ± 4.5	...	...	...
SC3	0.0013 ± 0.001	23.9 ± 1.1	7.1 ± 2.7	...	...	...
SC9	$(6.7 \pm 3) \times 10^{-6}$	26.4 ± 2.6	6.3 ± 2.7	...	...	...
C2	0.033 ± 0.03	16.3 ± 2.5	0.7 ± 0.4	...	...	...
C3	$(2.4 \pm 1) \times 10^{-5}$	19.5 ± 1.9	1.4 ± 0.6	...	...	...

NOTE.—Parameters for the 3-d and 2-d samples: ellipticity (e_λ), geometric-mean FWHM (θ_λ), and flux (S_λ) are given.

only at temperatures below $\sim$20 K (Bergin, Langer, & Goldsmith 1995), somewhat cooler than the clumps in the Lagoon Nebula.

3.3.1. *Gas Temperature*

The simplest method of estimating a gas temperature is to measure the peak brightness temperature in optically thick ^{12}CO. However, the unknown filling factor of the beam and the possibility of self-absorption undermine this technique. Also, since ^{12}CO is optically thick, the line may not be representative of the bulk of the column.

If spectra are available for a clump in two optically thin transitions (e.g., ^{13}CO and C^{18}O), the ratio of the two may be used to estimate the temperature (Myers, Linke, & Benson 1983). This technique avoids the problems of self-absorption and unknown filling factor, and, since the transitions are optically thin, the whole gas mass is sampled. However, it does require the assumption of an abundance ratio between ^{13}CO and C^{18}O, n_{13}/n_{18}. Myers et al. (1983) use solar abundances, giving $n_{13}/n_{18} = 5.5$. Langer & Penzias (1990) measured a gradient in ^{12}C/^{13}C ratio over the Galactic disk, with ^{13}C enhanced toward the center of the galaxy, and found that the local interstellar medium ^{12}C/^{13}C ratio is rather lower than the solar ratio of 89. Adopting a galactocentric distance of 8.3 kpc for M8, the Langer & Penzias (1990) relationship gives a ^{12}C/^{13}C ratio of $\sim$50; with a solar ^{16}O/^{18}O ratio of 500 (Zinner 1996), $n_{13}/n_{18} \approx 10$.

The gas excitation temperatures, estimated from ^{12}CO (T_{12}) and from ^{13}CO and C^{18}O ($T_{13/18}$), are given in Table 5, along with the estimated optical depth of the C^{18}O transition. M8E and M8SE estimates are based on 2–1 transitions, while all others used 3–2 spectra; T_{12} estimates for M8SE1 and 2 are based on 3–2 spectra, but $T_{13/18}$ estimates

TABLE 3
CO 3–2 Emission-Line Parameters

	^{12}CO			^{13}CO			C^{18}O		
Clump	T_R^* (K)	Δv (km s^{-1})	v (km s^{-1})	T_R^* (K)	Δv (km s^{-1})	v (km s^{-1})	T_R^* (K)	Δv (km s^{-1})	v (km s^{-1})
HG	94.1	3.8	9.8	38.9	3.2	9.8	11.9	2.3	9.3
WC1	39.6	5.1	8.8	19.9	2.5	8.6	4.2	2.3	8.0
WC2	31.8	4.8	9.4	16.5	2.5	9.0	5.3	1.6	8.5
WC3	37.8	3.3	10.2	16.2	2.7	10.4	...	...	...
WC4	58.1	2.4	11.4	21.3	1.8	11.7	...	...	...
WC5	47.7	3.1	10.4	8.6	3.7	9.4	...	...	...
WC6	45.0	2.2	10.4	9.3	4.3	9.7	3.7	2.5	8.2
WC7	27.8	1.3	12.7	13.4	1.4	12.8	7.0	0.5	12.9
WC8	21.1	4.0	9.6	7.2	2.0	9.2	...	...	...
WC9	16.6	4.3	9.5	5.4	2.8	10.0	...	...	...
SW1	19.1	2.8	9.4	...	...	...	...	...	...
EC1.....	39.0	3.2	14.6	17.2	2.1	14.8	5.2	1.2	14.8
EC2.....	49.4	2.1	12.3	27.1	1.7	12.5	8.7	1.2	12.4
EC3.....	55.9	1.9	12.8	28.4	1.5	12.8	15.0	1.0	12.6
EC4.....	45.6	3.5	16.2	20.9	2.1	16.3	5.0	1.4	16.6
EC5.....	51.0	2.1	17.0	23.5	1.5	17.0	8.6	1.0	17.1
SE1	61.7	2.2	13.5	34.2	1.6	13.5	...	...	...
SE2	55.8	2.9	13.9	27.9	1.8	13.9	...	...	...
SE3	49.3	2.5	12.6	...	...	...	...	...	...
SE4	42.0	3.1	13.1	...	...	...	...	...	...
SE5	39.0	2.2	12.5	...	...	...	...	...	...
SC1	61.5	2.5	10.3	30.6	1.6	10.1	13.1	0.9	9.8
SC2.....	43.1	2.4	9.9	20.7	2.4	9.7	9.9	1.6	9.5
SC3.....	31.1	1.4	9.7	9.5	3.5	9.6	5.9	1.4	9.0
SC4.....	32.5	1.6	10.8	13.6	1.9	11.0	4.0	0.9	10.6
SC5.....	44.1	2.2	12.1	19.8	2.0	12.5	...	...	...
SC6.....	29.2	2.3	12.7	12.7	1.8	12.7	2.8	0.9	12.4
SC7.....	37.3	3.6	11.5	12.1	1.5	11.5	...	...	...
SC8.....	51.2	2.7	12.5	29.2	2.2	12.5	12.2	1.4	12.5
SC9.....	43.3	2.4	13.0	18.7	1.6	13.4	...	...	...
C1	25.2	1.7	14.0	8.6	2.0	13.9	2.3	2.7	13.9
C2	51.8	2.3	12.3	20.4	1.5	12.2	3.0	2.3	11.7
C3	32.2	2.7	16.0	12.5	1.9	15.8	2.9	0.6	16.7

use 2–1. Formal errors in the excitation temperature estimates are derived from the uncertainty in the peak value of the Gaussian fit to the spectral line. All the JCMT on-the-fly maps have a noise of $\sim$2 K per channel. This was taken to be the error in the peak T_R^* for all isotopomers of CO 3–2, a conservative estimate, since it takes no account of the multiple channels used to fit a Gaussian to the line. Errors for the HHT 2–1 spectra use results from the fitting algorithm. Most clumps have C^{18}O optical depth τ_{18} of order 0.1, giving ^{13}CO optical depths of order unity, so the optically thin assumption is not strictly true. One effect of this is that increasing the isotopomer ratio n_{13}/n_{18} from 10 to 20 (as might occur in a photon-dominated region) reduces the derived temperature by an average of only 1.5 K.

TABLE 4
CO 2–1 Emission-Line Parameters for Southeastern Clumps

	^{12}CO			^{13}CO			C^{18}O		
Clump	T_{mb} (K)	Δv (km s^{-1})	v (km s^{-1})	T_{mb} (K)	Δv (km s^{-1})	v (km s^{-1})	T_{mb} (K)	Δv (km s^{-1})	v (km s^{-1})
SE1	...	...	...	17.4	1.8	13.6	6.1	1.1	13.6
SE2	...	...	...	22.1	1.5	13.9	4.5	1.2	13.9
SE3	38.3	2.6	12.5	15.4	1.6	12.7	4.5	1.5	12.8
SE4	32.0	2.2	12.3	13.3	1.7	12.2	2.8	2.4	12.4
SE5	30.6	2.2	12.2	12.9	1.6	12.0	2.1	3.2	11.8
SE6	32.9	2.2	10.8	13.8	1.5	10.6	2.6	1.2	10.7
SE7	38.0	2.4	10.0	24.0	1.8	10.0	6.6	1.1	9.9
SE8	44.4	2.9	10.3	23.0	2.4	10.3	6.6	1.8	10.0
E	35.4	4.3	10.9	23.5	3.0	10.8	9.9	2.3	10.8

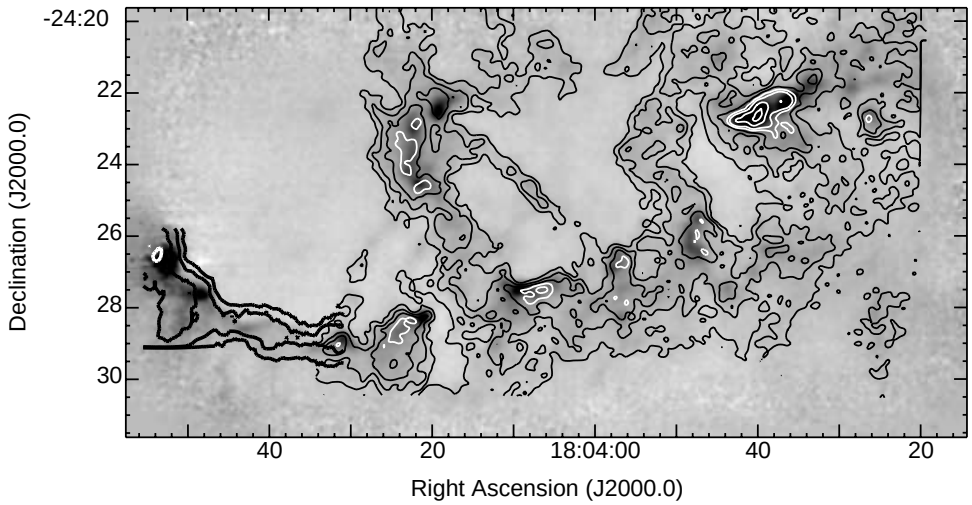

FIG. 5.—850 μm emission map (*grayscale*) with ^{12}CO maps overlaid. The thick contours are at values of ^{12}CO 2–1 integrated intensity of 25, 50, 100 K km s^{-1} (*black*) and 150 K km s^{-1} (*white*). The thin contours are at values of ^{12}CO 3–2 integrated intensity of 50, 100, 150 K km s^{-1} (*black*) and 200, 250, 350, 450 K km s^{-1} (*white*).

TABLE 5

MOLECULAR GAS PARAMETERS FROM CO LINE MEASUREMENTS

Clump	T_{12} (K)	$(\tau_{18})_{\rm min}$	τ_{18}	$(\tau_{18})_{\rm max}$	$T_{13/18}$ (K)	$T_{\rm adopt}$ (K)	log $N(H_2)$ (cm^{-2})	log $n(H_2)$ (cm^{-3})
HG	102.2 ± 2.0	0.28	0.35	0.46	$47.6^{+2.4}_{-0.8}$	47.6 ± 1.1	22.96 ± 0.12	5.27 ± 0.13
WC1	47.5 ± 2.0	0.08	0.20	0.53	$30.2^{+12.2}_{-3.0}$	30.2 ± 2.6	22.45 ± 0.52	4.71 ± 0.57
WC2	39.6 ± 2.0	0.23	0.38	0.76	$24.0^{+1.4}_{-0.4}$	24.0 ± 0.9	22.44 ± 0.28	4.55 ± 0.30
WC3	45.6 ± 2.0	...	...	...	...	25.1 ± 4.7	...	...
WC4	66.1 ± 2.0	...	...	...	...	36.4 ± 6.7	...	...
WC5	55.6 ± 2.0	...	...	...	...	30.6 ± 5.7	...	...
WC6	52.9 ± 2.0	0.27	0.50	3.02	$16.0^{+0.7}$	16.0 ± 0.4	22.62 ± 0.53	4.76 ± 0.57
WC7	35.5 ± 2.0	0.50	0.74	1.47	20.4	20.4 ± 0.1	22.16 ± 0.24	4.32 ± 0.26
WC8	28.6 ± 2.1	...	...	...	...	15.8 ± 3.1	...	...
WC9	24.0 ± 2.1	...	...	...	...	13.2 ± 2.7	...	...
SW1	26.6 ± 2.1	...	...	...	...	14.6 ± 2.9	...	...
EC1.....	46.9 ± 2.0	0.21	0.35	0.70	$24.9^{+1.9}_{-0.6}$	24.9 ± 2.3	22.30 ± 0.29	4.52 ± 0.33
EC2.....	57.3 ± 2.0	0.28	0.38	0.55	$35.1^{+1.2}_{-0.5}$	35.1 ± 0.5	22.52 ± 0.16	4.65 ± 0.18
EC3.....	63.9 ± 2.0	0.61	0.75	0.97	$35.8^{+0.1}$	35.8 ± 0.1	22.75 ± 0.10	4.90 ± 0.13
EC4.....	53.5 ± 2.0	0.13	0.25	0.52	$30.1^{+5.7}_{-1.8}$	30.1 ± 3.8	22.32 ± 0.36	4.52 ± 0.38
EC5.....	59.0 ± 2.0	0.33	0.45	0.67	$31.1^{+0.6}_{-0.3}$	31.1 ± 0.5	22.45 ± 0.16	4.59 ± 0.18
SC1.....	69.5 ± 2.0	0.45	0.56	0.72	$38.1^{+0.3}$	38.1 ± 0.2	22.61 ± 0.10	4.88 ± 0.15
SC2.....	51.0 ± 2.0	0.49	0.65	0.96	$28.0^{+0.1}_{-0.1}$	28.0 ± 0.1	22.76 ± 0.15	4.86 ± 0.17
SC3.....	38.9 ± 2.0	0.58	0.97	...	16.2	16.2 ± 0.1	22.65	4.88
SC4.....	40.3 ± 2.0	0.17	0.33	0.95	$21.1^{+2.0}_{-0.5}$	21.1 ± 1.5	22.09 ± 0.40	4.20 ± 0.42
SC5.....	52.0 ± 2.0	...	...	...	...	28.6 ± 5.3	...	...
SC6.....	36.9 ± 2.0	0.06	0.22	1.72	$21.3^{+15.5}_{-1.7}$	21.3 ± 8.6	21.91 ± 0.90	4.24 ± 0.92
SC7.....	45.1 ± 2.0	...	...	...	...	24.8 ± 4.6	...	...
SC8.....	59.2 ± 2.0	0.43	0.54	0.71	$36.7^{+0.4}_{-0.1}$	36.7 ± 0.2	22.77 ± 0.10	4.83 ± 0.15
SC9.....	51.2 ± 2.0	...	...	...	...	28.2 ± 5.2	...	...
C1	32.8 ± 2.0	0.08	0.29	...	$15.8^{+6.6}$	15.8 ± 6.6	22.41	4.66
C2	59.8 ± 2.0	...	0.09	0.60	$41.0_{-13.3}$	41.0 ± 16.1	22.29	4.61
C3	40.0 ± 2.0	0.07	0.24	1.58	$20.8^{+10.7}_{-1.4}$	20.8 ± 6.1	21.75 ± 0.78	4.11 ± 0.82
From ^{12}CO 2–1 Data								
E	40.7 ± 0.1	0.47	0.54	0.65	$28.6^{+0.1}_{-0.1}$	28.6 ± 0.1	23.09 ± 0.08	5.29 ± 0.08
SE1	...	0.31	0.42	0.65	$22.5^{+0.6}_{-0.2}$	22.5 ± 0.4	22.50 ± 0.18	4.64 ± 0.19
SE2	...	0.11	0.19	0.33	$31.0^{+7.2}_{-3.1}$	31.0 ± 5.2	22.41 ± 0.35	4.55 ± 0.39
SE3	43.6 ± 1.3	0.21	0.33	0.61	$20.8^{+1.7}_{-0.5}$	20.8 ± 1.1	22.47 ± 0.27	4.57 ± 0.28
SE4	37.3 ± 2.1	0.11	0.19	0.34	$20.5^{+4.8}_{-2.0}$	20.5 ± 2.4	22.42 ± 0.36	4.82 ± 0.40
SE5	35.9 ± 3.0	0.05	0.12	0.24	$23.2^{+14.5}_{-4.3}$	23.2 ± 9.9	22.44 ± 0.58	4.65 ± 0.60
SE6	39.2 ± 2.1	0.08	0.17	0.31	$21.9^{+7.4}_{-2.7}$	21.9 ± 5.1	22.11 ± 0.43	4.24 ± 0.45
SE7	36.1 ± 0.6	0.24	0.31	0.40	$30.1^{+1.2}_{-0.8}$	30.1 ± 1.0	22.56 ± 0.14	4.83 ± 0.16
SE8	49.7 ± 1.8	0.27	0.33	0.41	$28.7^{+0.8}_{-0.5}$	28.7 ± 0.7	22.77 ± 0.11	5.00 ± 0.14

The good correlation between T_{12} and $T_{13/18}$ can be used to estimate $T_{13/18}$ for clumps with ^{12}CO spectra but no ^{13}CO or C^{18}O: on the basis of a straight-line fit to the data, they are assumed to have $T_{13/18} = (0.55 \pm 0.1)T_{12}$. The systematically lower temperatures obtained from the rarer isotopomers may arise from the difference in optical thickness of the transitions. In general, ^{12}CO emission is expected to trace the surface of the cloud. If the cloud is externally heated, the ^{12}CO emission will arise from the warmer material at the surface, while ^{13}CO and C^{18}O emission is dominated by the cooler material inside. Since dust emission is optically thin, $T_{13/18}$ is likely to be a more accurate estimate of the dust temperature, and is used as the "adopted temperature" ($T_{\rm adopt}$) in Table 5.

The errors assigned to the adopted temperatures are half of the confidence interval. Since the analysis uses nonlinear relationships, the errors are not normally distributed, and the derived value need not be in the middle of the confidence interval, so these error values should be treated with caution. In the case of M8C2, the line temperature ratio (within the errors) is consistent with $\tau_{18} = 0$ and thus a very large gas temperature; the maximum temperature was taken to be T_{12}. In M8C1 and M8C3, the spectra are consistent with a line ratio less than unity, interpreted as both transitions being optically thick. The average temperature of all clumps measured in ^{13}CO and C^{18}O 3–2 is 27.3 K, with an rms scatter of 8.4 K (excluding the M8HG clump), and the average ^{12}CO 3–2 temperature of all measured clumps is 50.0 ± 12.3 K, equivalent to an average temperature $\overline{T}_{13/18} = 27.5 \pm 13.3$ K. Values of $T_{13/18}$ for the SE clumps measured in CO 2–1 are consistent with these averages.

3.3.2. *Gas Density*

The column density of C^{18}O can be derived from the optical depth of the transition, integrated over the line; divided by the fractional abundance of C^{18}O, this yields the column density of H_2. The abundance was taken to be $X(\mathrm{C^{18}O/H_2}) \approx 1.7 \times 10^{-7}$ (e.g., Goldsmith, Bergin, & Lis 1997; White et al. 1999), although this is highly uncertain. The integrated optical depth was approximated by $\int_{\rm line} \tau_{18} dv \approx \tau_{18}^0 \Delta v_{18}$; $T_{\rm adopt}$ was used as the excitation temperature. Maximum and minimum values of the column density were derived from the confidence limits on τ_{18}^0 and $T_{\rm adopt}$ (Table 5).

The volume density of molecular hydrogen $n(H_2)$ was obtained by assuming that the size of the clump along the line of sight is similar to its projected size on the plane of the sky, taken to be the FWHM of the clump at 850 μm. This assumes that the clumps are spherically symmetric, which need not be true. However, for a lack of spherical symmetry to cause a systematic error in the derivation of volume densities, the nonspherical clumps would have to be generally aligned. It was also assumed that there is no significant contribution to the C^{18}O emission by molecular gas outside the clump along the line of sight. Minimum and maximum volume densities were derived from the confidence limits on column density and on the FWHM at 850 μm. No account was taken of the additional random error estimated from the scatter in areas, but this error is low for 850 μm estimates. Both column and volume densities of H_2 are given in Table 5.

3.4. *Contamination in the Continuum Data*

3.4.1. *Free-Free Contamination*

Free-free emission from the ionized gas may be a significant component of the submillimeter continuum emission. However, large-scale smooth free-free emission is unlikely to contaminate most sources, due to a combination of low spatial frequency suppression by chopping and local background subtraction during the flux measurement. However, electron density enhancements might be associated with clumps in the molecular cloud, giving rise to significant contamination. The possible importance of free-free contamination may be estimated from the model of Lynds & O'Neil (1982). They postulate four (possibly overlapping) H II regions: the Hourglass and regions I, II, and III, ionized by (I) Her 36, (II) 9 Sgr, and (III) HD 165052; according to Woodward et al. (1986), both the Hourglass and the neighboring region (I) are ionized by Her 36.

Observations of the Hourglass Nebula at 5 GHz with the VLA have been used to model the ionized gas (Woodward et al. 1986), which coincides with the HG clump in the submillimeter maps to within a few arcseconds. The estimated free-free emission constitutes just 4% of the emission at 450 μm, a quarter of the emission at 850 μm, and three-quarters of the 1.3 mm emission. The deconvolved Gaussian FWHM of the HG clump at 1.3 mm is 16″, closer to the size of the compact H II region than to the size of the 850 μm clump. So, in the case of the Hourglass clump, free-free emission may have a significant effect on the submillimeter fluxes.

The other clumps may be contaminated by emission from regions I, II, and III. Region III is large and diffuse ($\sim 2^\circ$ or 60 pc diameter, $n_e \sim 1$ cm^{-3}), so it is likely that its free-free emission is removed (as discussed above). Region II, ionized by 9 Sgr ($n_e \sim 100$ cm^{-3}), is expected to have a diameter of 6.4 pc or $\sim 13'$ (Lynds & O'Neil 1982), similar to the diameter of the central cavity in the submillimeter maps. Since 9 Sgr is near the center of the cavity, this suggests that region II can be identified with the cavity bounded by molecular material. The clumps found inside the cavity (M8C) may be behind the H II region and thus affected by the free-free emission. However, most of the effect of the free-free emission should be removed on a scale of a few arcminutes. Region I, the more diffuse ($n_e \sim 250$ cm^{-3}) H II region ionized by Her 36, with an estimated diameter of 2.2 pc or $\sim 4'$, corresponds to the bright nebular region around the Hourglass (e.g., Elliot et al. 1984) and could affect most of the clumps in M8WC. Emission on this spatial scale will be imaged effectively in the submillimeter but may be removed by local background fitting.

There are a number of optically bright nebular features in the west of the M8 complex, such as the filaments of the Super Hourglass Structure (SHGS; Lada et al. 1976; Elliot et al. 1984), with increased electron density (Bohuski 1973). Given their scales of a few arcseconds ($\sim$0.1 pc), they should have emission measures of order 10^6 cm^{-6} pc (similar to that of the Hourglass) and may significantly contaminate the submillimeter fluxes of any clumps with which they coincide. M8C2 and M8WC4, 5, 6 may be affected in this way (see Elliot et al. 1984 for a S II image), and there is also S II emission at the edge of M8SC 8 (Lada et al. 1976); however, the latter is a very bright clump, so the contamination is unlikely to be serious.

It is possible to estimate the maximum free-free contribution due to the various H II regions in the Lynds & O'Neil

(1982) model (neglecting the effect of structures such as the SHGS). The electron temperature is assumed to be 5000 K for all regions (Bohuski 1973), somewhat lower than that derived by Woodward et al. (1986) for the Hourglass. The free-free emission should contribute a few times 0.01 Jy beam^{-1}, which may be important in the faintest clumps, and may even be dominant at 1.3 mm, depending on the extent to which it is filtered out by the imaging process. For most clumps, free-free emission is not a significant problem and has been neglected for all clumps except M8HG.

3.4.2. *Spectral Line Contamination*

Submillimeter spectral line radiation arising from molecular gas can contribute to the measured continuum flux: estimates of the fraction of continuum emission toward Orion OMC-1 at 1.3 mm that may be attributed to line emission range from 10% to 60% (Sutton et al. 1984; Greaves & White 1991; Oldham et al. 1994). Most of the area covered by the submillimeter continuum maps is also covered by the ^{12}CO 3–2 map, so the line contamination for all passbands was estimated from the ^{12}CO 3–2 line intensity, multiplied by a correction factor (the ratio between the total intensities of all astronomical lines within the continuum bandpass and the integrated intensity of the ^{12}CO line), estimated from spectral line surveys.

The 1.3 mm band was partially surveyed toward Orion KL by Sutton et al. (1985), Blake et al. (1986), and Greaves & White (1991). Applying a correction to account for the incompleteness with which they sample the 80 GHz bandwidth (assuming uniform line emission over the band), and excluding the broad shock-excited lines of SO and SO_2 seen toward Orion KL, the ratio of total line intensity to ^{12}CO line intensity $\int_{\rm band} T_A^* dv / \int_{\rm CO} T_A^* dv \sim 6$. Helmich & van Dishoeck (1997) carried out a spectral survey at 1.3 mm toward three sources in W3: IRS4, IRS5, and H_2O. These sources are much less rich than Orion, with estimated (bandwidth-corrected) intensity ratios of about 3, 3, and 5, respectively.

The spectrum of Orion KL has been surveyed in the 850 μm band by Schilke et al. (1997): excluding SO and SO_2 and correcting for bandwidth gives $\int_{850} T_R^* dv / \int_{\rm CO} T_R^* dv \sim 3$. Sutton et al. (1995) observed five positions around Orion KL, giving ratios (estimating ^{12}CO from the C^{17}O transition) ranging from 2 to 6. Sutton et al. (1991) conducted a spectral survey of Sgr B2(M), giving $\int_{850} T_R^* dv / \int_{\rm CO} T_R^* dv \sim 3$. The Helmich & van Dishoeck (1997) survey toward W3 IRS4, IRS5, and H_2O also covered 28 GHz of the 850 μm band: the derived intensity ratios are about 2, 2, and 3, respectively.

These surveys tend to concentrate on rich sources of interstellar molecular lines and on relatively rich parts of the spectrum, suggesting that the factors derived here are upper limits. Limited spectral line observations show that the clumps around the Lagoon Nebula are not particularly rich in lines, nor do they show very strong SO or SO_2 emission. In the 850 μm passband, a correction factor of 2–3 seems reasonable and 5 would be an upper limit. In the much wider 1.3 mm band, a correction factor of 3–5 is consistent with the survey data.

The integrated intensity of the ^{12}CO 6–5 line at 690 GHz and ^{12}CO 2–1 (230 GHz), and hence the line contribution to the 450 μm and 1.3 mm fluxes, can be estimated from the ^{12}CO 3–2 line. Serabyn & Weisstein (1995) found that the ^{12}CO lines toward Orion IRc2 (up to 7–6) have frequency-integrated intensities $\int T_R^* d\nu \propto \nu$, but that transitions of other molecules tend to have constant frequency-integrated intensities. The ^{12}CO 3–2 and 2–1 data for M8 follow the rule for Orion IRc2, but the molecular gas in M8 may not be hot enough for this to extend as far as ^{12}CO 6–5.

The ^{12}CO 3–2 integrated intensity map is rather smooth compared to the continuum maps, suggesting that some of the ^{12}CO emission in spectra toward the clumps will be included in the fitted background, rather than the Gaussian fits. The ^{12}CO intensity can also be estimated by comparing the value at the clump with the local background. Estimates of the likely spectral line contamination in the various continuum passbands were all extrapolated from the integrated intensity of ^{12}CO 3–2: 20%–60%, 45%–150%, and 10%–45% at 850 μm, 1.3 mm, and 450 μm, respectively. Despite the large uncertainties, it seems that line contamination is likely to be a significant problem at 1.3 mm, whereas in the SCUBA 450 μm and 850 μm bands, it could be as low as 10% (an insignificant error) or as high as a half. M8SE3, M8C2, M8C3, M8SC7, M8WC4, and M8WC5 have consistently high estimates of line contamination and may even be dominated by line emission.

3.4.3. *Dust Emission from* H II *Regions*

Dust grains survive inside H II regions and produce their own graybody emission, which could contaminate the submillimeter flux measurements of clumps behind the H II region. The strongest emission is likely to arise toward M8WC, which, in the Lynds & O'Neil (1982) model, lies behind the largest column of ionized gas. Woodward et al. (1986) found $A_V \approx 1$ toward the Hourglass, corresponding to $\tau_{100} \approx 4 \times 10^{-3}$ at 100 μm (Harvey, Thronson, & Gatley 1980). Assuming $\beta = 2$ for bare grains in an H II region (Draine & Lee 1984; Hobson et al. 1993; Ristorcelli et al. 1996), the optical depths at 450 μm, 850 μm, and 1.3 mm are 10^{-4}, 2×10^{-5}, and 10^{-5}. Adopting a dust temperature of 60 K (Soifer, Pipher, & Houck 1972), the estimated submillimeter fluxes in the beam are 0.2 Jy beam^{-1}, 0.02 Jy beam^{-1}, and 0.003 Jy beam^{-1} respectively, small enough to be neglected.

3.4.4. *Dust Emission from Photodissociation Regions*

If a clump is exposed to UV radiation, the cool clump core is shielded by a warmer layer or photodissociation region (PDR); if the continuum radiation from the thin warm PDR were to constitute a substantial fraction of the flux from the clump, then the analysis of the submillimeter emission would be affected. The temperature structure of the dust in clumps and the PDRs at their surfaces has been modeled by Hollenbach, Takahashi, & Tielens (1991): the dust in the clump may be considered to be at an "asymptotic temperature" T_a, except for a thin surface layer at temperature T_0. The UV flux incident on the clumps in M8 can be estimated by adding the contributions of the two stars presumed to dominate the region: Her 36 (O8 V) and 9 Sgr (O4 V), using published stellar atmosphere models (Kurucz 1979), and neglecting projection effects in the map.

The estimated PDR temperature T_0 is correlated with the ^{12}CO gas temperature: M8HG and the clumps in M8WC and M8C have $T_0 \approx T_{12}$, while the clumps in M8EC, M8SC, M8SW, and M8SE generally have lower T_0 than T_{12}

(although they are still correlated). This suggests that clumps in the latter regions are exposed to substantially more UV flux than estimated, presumably from other stars in the cluster NGC 6530, found in front of the eastern part of the complex. The submillimeter emission was estimated by taking $T_0 = T_{12}$, and using the Hollenbach et al. (1991) model to calculate T_a from T_0. For most of the clumps, the PDR flux is $\leq$20% of the clump flux, but six clumps have high contamination (>20%): M8EC1, M8SC6, M8SC4, M8C1, M8WC7, and M8C3; this is due to the relatively low column densities of these clumps—six out of the eight lowest estimates of $N(H_2)$. The mass of a PDR is largely determined by the UV flux; hence a lower mass clump will be more dominated by PDR emission than a higher mass one.

Contamination from hot dust in PDRs is not a grave problem for the clump sample; at around 10%–20% it is more significant than calibration error, but less so than line contamination. The level of contamination in individual beams can be rather higher, so the PDRs may affect the map toward the edge of the clumps, which may in turn affect the Gaussian-fitting process.

3.5. *Physical Properties of Clumps*

3.5.1. *Temperature and Emissivity*

Ratios of the peak brightnesses of the clumps in the different wave bands can be used to characterize the physical properties of the emitting dust. These ratios are used in preference to ratios of the integrated fluxes because of the large uncertainties in the latter due to errors in the fitted area. Even so, the uncertainties are large enough that it is not possible to derive both $T_{\rm dust}$ and β solely from continuum observations. Estimating the dust temperature from CO data, the continuum data can be used to derive an average emissivity index $\overline{\beta}$ for the whole clump sample. The gas and dust are not expected to be well coupled below volume densities $n(H_2) > 10^5$ cm^{-3} (White et al. 1999), somewhat higher that the typical volume densities of the M8 clumps. Nevertheless, using the estimated gas temperature should be a better approximation than guessing a blanket temperature for the entire region.

Estimates of β are given in Table 6: for the 3-d sample, $\beta_{\rm short}$ (between 450 and 850 μm) and $\beta_{\rm long}$ (between 850 μm and 1.3 mm) were derived; an overall estimate was obtained by fitting a straight line to all three data points and is given together with the estimated error in $\beta_{\rm fit}$, σ_β, and the χ^2 of the fit. For the 2-d sample, only $\beta_{\rm short}$ is given. The overall average of $\beta_{\rm short}$ and $\beta_{\rm long}$ for both samples is $\beta = 1.4 \pm 0.3$; this is consistent with the average value of $\beta_{\rm fit}$ and with the averages of all the subsamples. The Hourglass clump, M8HG, was excluded from the averages, since it was likely to be highly contaminated by free-free emission; this is supported by low estimates of β.

To what extent might the observed value of β be affected by the various forms of contamination considered above? Free-free emission may be important in M8HG, but the distributions of $\beta_{\rm short}$ and $\beta_{\rm long}$ for the rest of the 3-d sample are quite consistent with one another. This suggests that free-free emission has a negligible effect on the spectral index. The effect of hot dust, whether in the H II regions of the complex or in PDRs, is unlikely to be serious, since it is also graybody dust emission. However, the dust in these regions is exposed to high UV fluxes and is presumably composed of bare grains ($\beta \approx 2$). If the aggregated ice-mantled grains expected to make up the clumps has $\beta < 2$, then the effect of the hot dust will lead to an overestimate of β, but the low levels of contamination render this error negligible.

TABLE 6
GRAYBODY INDICES

Clump	$\beta_{\rm short}$	$\beta_{\rm long}$	$\beta_{\rm fit}$	σ_β	χ^2
		3-d Sample			
HG	1.02 ± 0.09	0.46 ± 0.14	0.60	0.16	1.31
WC1	1.86 ± 0.26	1.36 ± 0.38	1.48	0.67	0.08
WC2	1.68 ± 0.22	1.32 ± 0.24	1.38	0.34	0.52
EC1.....	0.86 ± 0.25	1.75 ± 0.31	1.05	0.36	2.48
EC3.....	1.22 ± 0.16	1.08 ± 0.19	1.01	0.15	2.84
EC4.....	1.33 ± 0.16	1.40 ± 0.13	1.20	0.41	0.81
SE1	1.21 ± 0.22	1.52 ± 0.14	1.22	0.40	1.49
SE2	0.50 ± 0.21	0.72 ± 0.26	0.41	0.37	0.98
SE3	1.46 ± 0.17	1.33 ± 0.14	1.25	0.39	0.70
SC1	1.97 ± 0.23	1.47 ± 0.34	1.59	0.17	0.64
SC2	1.75 ± 0.16	1.18 ± 0.11	1.38	0.20	0.90
SC4	1.61 ± 0.20	1.84 ± 0.24	1.54	0.45	1.00
SC5	1.70 ± 0.18	1.10 ± 0.18	1.30	0.40	0.18
SC6	2.07 ± 0.40	0.85 ± 0.31	1.41	1.05	0.0002
SC7	1.07 ± 0.17	2.46 ± 0.31	1.39	0.45	3.30
SC8	1.39 ± 0.16	1.88 ± 0.29	1.32	0.20	5.74
C1	1.72 ± 0.44	1.44 ± 0.32	1.47	0.88	0.09
		2-d Sample			
WC3	1.83 ± 0.22	...	...	...	...
WC4	0.31 ± 0.28	...	...	...	...
WC5	1.63 ± 0.31	...	...	...	...
WC6	1.26 ± 0.33	...	...	...	...
WC7	1.53 ± 0.22	...	...	...	...
WC8	2.17 ± 0.31	...	...	...	...
WC9	2.32 ± 0.45	...	...	...	...
SW1	1.94 ± 0.47	...	...	...	...
EC2.....	1.65 ± 0.26	...	...	...	...
EC5.....	1.34 ± 0.12	...	...	...	...
E	1.64 ± 0.43	...	...	...	...
SE4	2.25 ± 0.34	...	...	...	...
SE5	1.59 ± 0.19	...	...	...	...
SE6	1.54 ± 0.49	...	...	...	...
SE7	1.50 ± 0.51	...	...	...	...
SE8	1.86 ± 0.55	...	...	...	...
SC3	2.28 ± 0.24	...	...	...	...
SC9	0.79 ± 0.24	...	...	...	...
C2	0.89 ± 0.46	...	...	...	...
C3	1.03 ± 0.44	...	...	...	...

NOTE.—Indices for clumps at short wavelengths (450 and 850 μm), at long wavelengths (850 μm and 1.3 mm), and fitted to all three wave bands, for 3-d and 2-d samples.

Contamination by spectral lines is potentially more serious. Line emission will appear to have an emissivity index $\beta_{\rm line}$ between 0.5 and 1.5. Of the three clumps considered likely to be dominated by line emission—SE2, C2, and C3—SE2 (in the 3-d sample) has $\beta < 1$ for all estimates (see Table 6); C2 and C3 (in the 2-d sample) both have fairly low estimates ($\beta_{\rm short} \approx 1$). Of the other three clumps that may have high levels of line contamination (SC7, WC4, and WC5), only WC4 has a particularly low value of β (<0.6), which, if accurate, could imply very high levels of line contamination. The values of SE2, C2, and C3 suggest that $\beta_{\rm line} \leq 1$. Thus the true β of the dust could be as high as 2, if the line contamination were very high (about half of the flux). Conversely, if the dust has $\beta = 1.5$, the spectral line contamination could be very low (~10%). Therefore

$\beta = 1.4 \pm 0.3$ may well be a systematic underestimate. However, this is compatible with previous studies (e.g., White et al. 1999) and with some theoretical models of dust emissivity. It is, of course, also possible that the true emissivity index of the dust varies from clump to clump, although there is no evidence for systematic variations in the data presented here.

3.5.2. *Mass*

The conversion of submillimeter flux to dust mass depends on the submillimeter opacity of the dust in each wave band, which in turn depends on a benchmark opacity at 400 μm (κ_{400}) and the wavelength dependence given by β. The value of κ_{400} is taken to be 10 cm^2 g^{-1} for dust alone; this value—higher than the canonical value (Hildebrand 1983) but roughly in line with theoretical models (Ossenkopf & Henning 1994; Krügel & Siebenmorgen 1994)—is uncertain by at least a factor of 2, but inaccuracy in it leads to systematic errors. The flux and opacity index were corrected for line contamination only: the ^{12}CO emission in each wave band was taken to be $\sim$15% of the continuum emission, using estimates of the ^{12}CO intensity above the local background. This gives fractional line contamination of 0.3 ± 0.15 at 450 and 850 μm and 0.45 ± 0.15 at 1.3 mm. If the spectral line emission has $\beta_{\rm line} = 0.75 \pm 0.25$, the true β of the dust emissivity is estimated to be 1.7 ± 0.5. Hence the dust opacities are $\kappa_{450} = 8.4$ cm^2 g^{-1}, $\kappa_{850} = 2.7$ cm^2 g^{-1}, and $\kappa_{1.3} = 1.3$ cm^2 g^{-1}. The error in β produces errors in the assumed opacities at different wavelengths, so that mass estimates from different wavelengths may be systematically different. Assuming a gas-to-dust ratio of 100, the total clump mass is given by

$$\frac{M}{M_\odot} = 4.788 \times 10^5 \frac{(D/\mathrm{pc})^2}{B(\nu, T_d)\kappa_{400}} \left(\frac{\lambda}{400\ \mu\mathrm{m}}\right)^{\beta} S_\nu(\lambda)\ . \quad (1)$$

The mass estimates for each clump, based on the various fluxes, are given in Table 7, together with the error-weighted average mass estimate. The error in the mass is based on the estimated flux error. The other source of error is uncertainty in the dust temperature, which gives an error in $\log M$ of order 0.1. The process of cross-referencing clump detections to allow accurate comparisons between different wave bands has the side effect of removing many clumps from the sample and hence impairing the completeness. Analysis of the mass distribution of clumps therefore used the complete lists of detections at 450 and 850 μm. Rather than averaging the results from the two bands to derive an average mass for each clump (which relies on the cross-referencing of the samples), the two lists were treated as being independent samples of the same underlying distribution of clumps; K-S tests show that the mass distributions in different wave bands are consistent with one another. The sample size is then $N = N_{450} + N_{850}$. All clumps were taken to have a temperature of 27 ± 13 K, since the submillimeter detections could not necessarily be securely identified with a given clump.

Figure 6 shows a histogram of the mass distribution of the full clump lists at 450 and 850 μm: if there are ΔN clumps in each bin of $\Delta \log M$, the histogram ordinate is given by $\log(\Delta N/\Delta M)$, where ΔM is the linear mass interval corresponding to the logarithmic interval $\Delta \log M$. If the clumps follow a mass function $dN/dM \propto M^{-\alpha}$, the histogram will follow a straight line of gradient $-\alpha$. At high masses ($\log M \gtrsim 1$), the function follows a straight line, consistent with a power-law mass function. The distribution flattens out at lower masses: in the absence of any very clear evidence that this effect is physical, the simplest explanation is that incompleteness becomes a problem below $\sim$10 $M_\odot$. It is not possible to estimate the completeness limit directly; it appears from the histogram that the distribution changes gradient at the histogram bin centered on $\log M/M_\odot = 0.8$. This was taken to be the completeness limit; power-law functions were fitted to the mass distribution using only detections with derived masses greater than $\log M/M_\odot = 0.8$.

K-S tests were used to assess the consistency between the distribution of the clumps and model power-law mass functions; this avoids the undesirable side effects of binning a small sample (Testi & Sargent 1998). The K-S probability $P_{\rm KS}$ was derived for a grid of possible values of the power-law index α (Fig. 6) and peaks at $\alpha = 1.66$. A 67% confidence interval can be estimated from $P_{\rm KS}(\alpha)$: the limits are the values of α for which $P_{\rm KS}$ is 17% of its peak (since the KS test is one-tailed). The limits $\alpha_{\rm max}$ and $\alpha_{\rm min}$ are 2.06 and 1.15, giving $\alpha = 1.66 \pm 0.45$. Model distributions for $\alpha_{\rm max}$ and $\alpha_{\rm min}$, and for the fitted value of α, are overlaid on the data in Figure 6.

Uncertainties in the masses may affect the power-law fitting. This possibility was investigated by Monte Carlo resampling: each clump detection was replaced by a random value sampled from a normal distribution, with the mean taken to be the estimated mass, and the standard deviation given by the estimated error. An additional error was applied to take into account the temperature uncertainty, taking the form $\Delta \log m$, normally distributed about zero, with standard deviation equivalent to 13 K. $P_{\rm KS}(\alpha)$ was averaged over 1000 simulated clump mass distributions to obtain $\overline{P}_{\rm KS}(\alpha)$, which, analyzed in the same way as above, gives $\alpha = 1.69 \pm 0.45$. So the mass errors do not greatly affect either the fitted value of α or even the width of the confidence interval. However, $\overline{P}_{\rm KS}(\alpha)$ is much lower for all α than $P_{\rm KS}$ without Monte Carlo resampling, so the unaltered estimates appear to be a better fit to a power law than the average resampled distribution.

4. DISCUSSION

4.1. *The Structure of the Lagoon Nebula*

The Lagoon Nebula consists of a number of H II regions in front of a molecular cloud (Lada et al. 1976; Lynds & O'Neil 1982). The continuum emission maps presented here tend to show the interfaces between H II regions and molecular cloud (since continuum emission traces dust temperature as well as column density), taking the form of dense clumps surrounded by more tenuous emission. The basic visual morphology of the map is rather variable: the "rim" connecting the SE clumps seems to be very sharply bounded on the side facing the interior of the nebula, whereas much of the emission in more central regions seems to have far shallower gradients. Measuring the 850 μm map gives some support to this: in places the SE rim emission falls off to half its peak value in about 10″, which would be consistent with the boundary being unresolved. Similarly sharp gradients may be found, e.g., near SC8. Shallower edges occur throughout the central parts of the map, e.g., near C2 and EC2, where it takes $\sim$20″ for the emission to fall by half.

TABLE 7
ESTIMATED GAS MASSES

Clump	M_{450} ($M_\odot$)	M_{850} ($M_\odot$)	$M_{1.3}$ ($M_\odot$)	$\overline{M}/M_\odot$
		3-d Sample		
HG	9.00 ± 3.87	14.23 ± 3.53	23.96 ± 7.21	13.26 ± 5.14
WC1	20.28 ± 8.70	9.52 ± 3.22	7.87 ± 2.98	9.32 ± 5.63
WC2	16.22 ± 7.43	15.54 ± 4.40	18.74 ± 6.18	16.54 ± 6.13
EC1.....	5.38 ± 2.45	10.97 ± 3.68	8.21 ± 3.08	7.43 ± 3.11
EC3.....	5.14 ± 2.34	7.59 ± 2.20	13.35 ± 4.48	7.22 ± 3.18
EC4.....	14.28 ± 6.14	14.89 ± 3.79	12.25 ± 3.75	13.67 ± 4.70
SE1	7.18 ± 3.36	16.12 ± 3.89	10.81 ± 3.19	10.92 ± 3.49
SE2	1.31 ± 0.56	4.85 ± 1.46	7.60 ± 2.62	1.98 ± 1.76
SE3	13.80 ± 6.03	16.27 ± 4.00	9.99 ± 2.98	12.44 ± 4.52
SC1	10.97 ± 4.80	3.05 ± 1.15	2.74 ± 1.13	3.11 ± 2.92
SC2	12.56 ± 5.64	11.03 ± 2.85	16.37 ± 5.06	12.36 ± 4.67
SC4	7.24 ± 3.12	8.76 ± 2.26	5.71 ± 1.76	6.93 ± 2.45
SC5	2.24 ± 0.98	2.04 ± 0.55	3.05 ± 0.97	2.27 ± 0.86
SC6	7.16 ± 3.22	2.71 ± 0.71	5.09 ± 1.59	3.27 ± 2.11
SC7	1.73 ± 0.74	3.69 ± 0.91	1.31 ± 0.39	1.70 ± 0.71
SC8	16.41 ± 7.36	22.26 ± 7.19	9.68 ± 3.53	12.79 ± 6.28
C1	5.99 ± 2.57	4.56 ± 1.27	1.93 ± 0.63	2.61 ± 1.69
		2-d Sample		
WC3	5.70 ± 2.52	1.97 ± 0.56	...	2.15 ± 1.83
WC4	0.70 ± 0.38	4.98 ± 1.23	...	1.08 ± 0.91
WC5	2.42 ± 1.19	2.03 ± 0.72	...	2.14 ± 0.99
WC6	5.64 ± 2.49	14.45 ± 4.54	...	7.69 ± 3.66
WC7	11.38 ± 5.32	12.83 ± 3.22	...	12.44 ± 4.40
WC8	25.34 ± 11.26	16.33 ± 4.00	...	17.34 ± 8.45
WC9	17.26 ± 7.85	7.66 ± 2.19	...	8.35 ± 5.76
SW1	6.19 ± 2.83	9.09 ± 3.35	...	7.40 ± 3.10
EC2.....	8.08 ± 4.19	4.94 ± 1.22	...	5.19 ± 3.08
EC5.....	4.75 ± 2.06	7.25 ± 1.86	...	6.13 ± 1.96
E	24.51 ± 10.60	43.30 ± 10.37	...	34.12 ± 10.49
SE4	4.06 ± 1.75	0.84 ± 0.29	...	0.93 ± 1.25
SE5	5.56 ± 2.39	4.62 ± 1.14	...	4.79 ± 1.87
SE6	5.85 ± 2.58	6.74 ± 1.72	...	6.47 ± 2.20
SE7	14.93 ± 6.92	11.79 ± 3.04	...	12.30 ± 5.34
SE8	6.42 ± 2.97	5.12 ± 1.62	...	5.42 ± 2.39
SC3	11.52 ± 5.01	7.42 ± 2.06	...	8.01 ± 3.83
SC9	3.41 ± 1.62	13.16 ± 3.68	...	5.00 ± 2.84
C2	0.20 ± 0.11	0.48 ± 0.21	...	0.27 ± 0.17
C3	1.31 ± 0.62	1.65 ± 0.54	...	1.50 ± 0.58

NOTE.—Masses of clumps from fluxes at 450 μm, 850 μm, and 1.3 mm and average masses. The errors are due to the estimated errors in the fluxes, and the error in the average mass is the standard deviation of the mean.

These differences in morphology may be caused by similar structure (molecular gas with a sharp edge where it meets the H II region and gentler gradients elsewhere) being viewed from a variety of angles.

The ionization of the Lagoon Nebula is generally ascribed to 9 Sgr and Her 36, but other OB stars in the Sgr 1A OB association may contribute as well, particularly in the eastern half of the complex. The observed temperatures of ^{12}CO in the eastern clumps suggest that more UV flux is incident on these clumps than can be accounted for by 9 Sgr, and this excess could be provided by the young cluster NGC 6530. M8SE forms a long loop in this region, linking a number of dense clumps with sharp edges pointing toward the center of the nebula, including the young stellar object M8E, which is the only confirmed locus of ongoing star formation in the complex.

The bulk of M8 is the "working surface" of the H II region of 9 Sgr expanding into the underlying molecular cloud (Dufour 1994). In the outer parts of the nebula (e.g., south of M8SC), less intense optical emission is seen, probably arising from the "champagne flow" of the H II toward the observer. The sharp-edged structure M8SC may be the southern rim of the crater excavated by 9 Sgr. M8SE follows the line of M8SC, but it appears to be focused on the cluster NGC 6530 rather than on 9 Sgr. This could be explained by both regions being originally part of the same structure in the molecular cloud but now being influenced by the radiation fields from different stars. The less sharp-edged features, such as M8EC and M8C, could be interpreted as clumps embedded in the cloud/H II region interface, like the rim structures, but seen face-on rather than edge-on. The Hourglass is embedded in the molecular cloud behind the

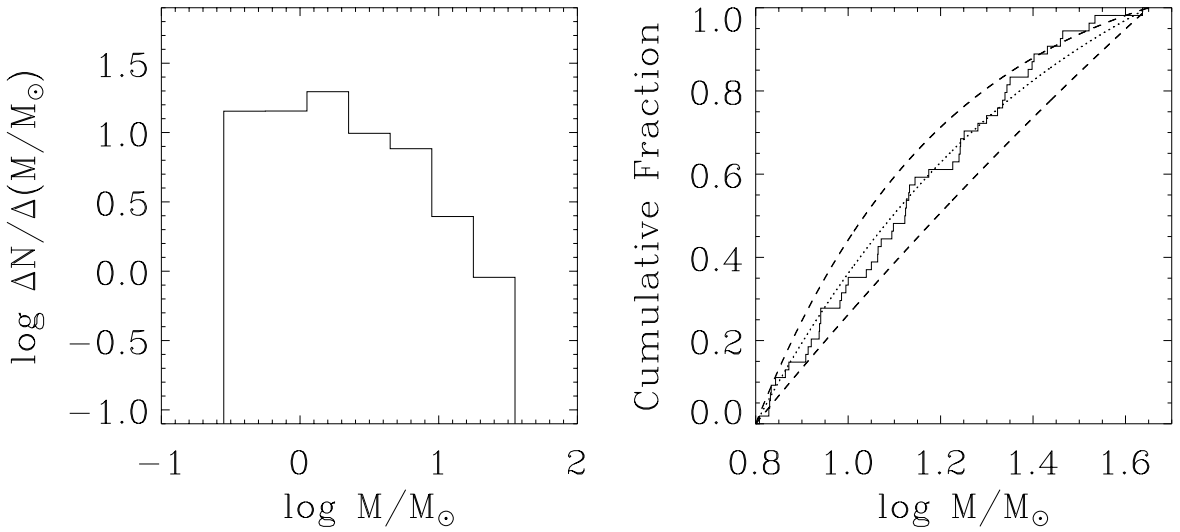

FIG. 6.—*Left*: The mass function of all clumps detected at 450 μm or 850 μm. *Right*: The cumulative distribution function of clump mass above $\log M/M_{\odot} = 0.8$, together with model cumulative distribution functions for mass functions with $\alpha = 1.66$ (*dotted line*) and $\alpha = 2.06,\ 1.15$ (*upper and lower dashed lines, respectively*).

H II region, close enough to the surface for part of it to be optically visible (Woodward et al. 1986); this is consistent with its association with M8WC, which appears to be a background structure. M8E, an even younger object, appears to be on the rim.

4.2. *The Mass Spectrum of the Lagoon Nebula*

The estimate above of the slope of the mass spectrum ($\alpha = 1.69 \pm 0.45$) ignores the statistical effect of the sample size (Williams et al. 1994; Elmegreen 1999): ~150 detections over the two SCUBA bands. The number of independent detections is smaller; this may seem inconsistent with the assertion above (§ 3.5.2) that the samples in the two wave bands are independent of one another. However, there are two separate statistical questions being asked; one concerns the estimates of the masses of the set of true clumps comprising the molecular cloud: what power-law best fits these estimates? In this case, the two data sets are independent estimates of the true masses of the real clumps, even if the same clump's mass is estimated twice, at different wavelengths. The second question concerns the relationship of the real clumps to the notional underlying mass distribution from which these real clumps are sampled. In this case, if the same clump is measured twice, it still represents only one sampling of the underlying mass spectrum. Therefore the effective sample size is only ~75, giving rise to an additional rms error of 0.4–0.5 in α; the final estimate is $\alpha = 1.7 \pm 0.6$.

This result is entirely consistent with previous determinations on a similar spatial scale, all of which used molecular line emission as a mass tracer. The recent higher resolution results (Motte et al. 1998; Testi & Sargent 1998; Johnstone et al. 2000; Motte et al. 2001), with their significantly larger exponents, were obtained using continuum mapping. Comparing these results with those of Heithausen et al. (1998), Motte et al. (2001) argue that continuum emission traces a different kind of structure to ^{12}CO; this argument could perhaps also be applied to studies using ^{13}CO, whose optical depth can be of order 1 in molecular clumps (see, e.g., Table 5). Continuum mapping also collapses the velocity axis of the data, giving a spatial map only, which might make it more difficult to distinguish weak peaks and hence bias the continuum mass spectrum to high masses. This study suggests that continuum-traced mass spectra are fully commensurable with their molecular line counterparts, at least at the spatial resolution of this study (about 0.1 pc). This still allows for a modified version of the Motte et al. (2001) argument: continuum mass spectra may trace a form of structure that changes its power-law index on small scales, while ^{12}CO may trace fully self-similar structure. Elmegreen et al. (2000) note that the masses of open clusters and OB associations are observed to follow power laws with exponents in the range 1.5–2, as opposed to the Salpeter initial mass function's exponent of 2.3. Given that the clumps examined in this work have similar size scales to young embedded clusters, it may be that the smaller exponent at the greater than 0.1 pc scale is linked to the mass spectrum of clusters, as the mass spectrum of the smaller clumps in Motte et al. (1998) and Testi & Sargent (1998) may be related to the initial mass function of stars. This would be fully consistent with the argument that continuum mapping traces the bound material that forms stars, as opposed to the component dominated by turbulence (Motte et al. 2001).

Alternatively, the inconsistency may lie in the fact that, in the ^{12}CO study of the Polaris Flare, the virial masses exceed the estimated masses by an order of magnitude, whereas the continuum studies all concentrate on star-forming regions, in which clumps are often gravitationally bound—in other words, the discrepancy may lie not in the tracer but in different regions having inherently different structure. It would be particularly interesting to derive mass spectra for the M8 complex over a large range of size scales to look for changes in the power-law index. Unfortunately, it is not easy to trace the Lagoon Nebula structure down to the ~0.01 pc level (as with ρ Ophiuchi, Serpens, and Orion B) due to its distance; angular resolution of ~1″ would be required, which is achievable only by aperture synthesis.

4.3. *The Evolution of the Lagoon Nebula*

The Lagoon Nebula is clearly a site of recent star formation, and there is ongoing star formation in M8E. The

clumps surrounding the H II region are obvious candidates to be the sites of a further generation of young stars, possibly by compression of the molecular gas by an ionization front (Spitzer 1978; Bertoldi 1989; Bertoldi & McKee 1990). When the ionizing flux of the OB stars hits a dense clump, it sets up a slow (D-type) ionization front (IF) and drives a shock front ahead of the IF, compressing the molecular gas. At the trailing edge of the IF, the gas recombines and is reionized by the incident flux, shielding the clump and increasing the timescale on which it is photoevaporated (Bertoldi 1989, and references therein). The interface between H II region and clump consists of the following layers: the H II region; the boundary layer, denser but still ionized; the IF; dense shocked gas; the shock front; and finally, the unshocked molecular gas of the original clump structure. The evolution of the molecular clumps was interpreted using the models of Bertoldi (1989) and Bertoldi & McKee (1990), adapted to the specific circumstances of the Lagoon Nebula (Tothill 1999).

4.3.1. *Pressure Balance*

The estimated internal and external pressures for the clumps in the 3-d and 2-d samples are shown in Figure 7. Correcting for the fact that the thermal component of the $C^{18}O$ line width underestimates the thermal line width of a mean molecule, the internal pressure is given by $P_{\rm int}/k = n_0(370\sigma_v^2 + 0.91T)$, where $P_{\rm int}/k$ has units of cm^{-3} K, σ_v is given by the FWHM in km s^{-1} divided by $(8\ln 2)^{1/2}$, and n_0 is the number density of molecules. If the nonthermal component is dominated by turbulent Alfvén waves, then the internal pressure could be up to 50% higher than this estimate (Myers & Goodman 1988; McKee & Zweibel 1995).

The external pressure (i.e., the pressure exerted by the shocked gas on the unshocked clump material) is given by $(P_{\rm ext}/k)/{\rm cm}^{-3}\ {\rm K} = 2.45 \times 10^7 (S_{49}/r_c R_*^2)^{1/2}$, where S_{49} is the Lyman flux of the star in units of 10^{49} photons s^{-1}, r_c and R_* are the radius of the clump and the distance from the clump to the star. This is the formula given by Bertoldi & McKee (1990) for an electron temperature of $\sim 10^4$ K; a temperature of 5000 K will reduce the pressure by $\sim$30%. The Lyman fluxes of the two OB stars thought to dominate the region are taken from Panagia (1973): 8.51×10^{49} photons s^{-1} from 9 Sgr (O4) and 2.24×10^{48} photons s^{-1} from Her 36 (O8).

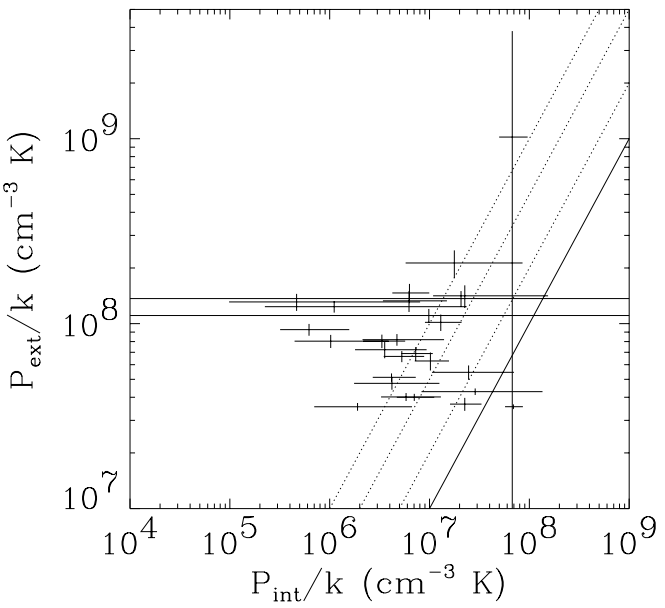

FIG. 7.—Estimated external and internal pressures on clumps. The solid line marks the locus where the pressures are equal. The broken lines correspond to external pressures 2, 5, and 10 times the internal pressures.

The total external pressure on the clump is obtained by summing the pressures due to each OB star. This is likely to overestimate the true pressure, because the pressure derived by considering the effect of one OB star does not take account of the attenuating boundary layer set up by the flux of the other star. This will be significant only if the clump receives comparable fluxes from the two stars, in which case the flux will be underestimated by a factor of $\sim$2 and the pressure overestimated by $\sim$40%. The plotted error bars are based on the uncertainty in the projected distance between star and clump, assumed to be similar to the clump size. No account was taken of projection effects, which will tend to reduce the incipient flux, and hence the external pressure, probably by a factor of about 2. A substantial contribution to the UV flux from other OB stars, particularly in the vicinity of NGC 6530, would increase the external pressure.

These uncertainties suggest that external pressures may be overestimated by factors of up to $\sim$4, but, even given this uncertainty, the external pressure is systematically higher than the internal pressure. This lack of equilibrium suggests that the shock front has not penetrated far, consistent with the narrow CO lines toward the clumps.

4.3.2. *Clump Mass and Gravitational Stability*

The critical Bonnor-Ebert mass $M_{\rm BE}$ is the maximum mass for which a clump is stable to gravitational collapse, equivalent to the Jeans mass with the addition of external pressure, given by

$$M_{\rm BE} = \frac{1.18\sigma_v^4}{G^{3/2}P_{\rm ext}^{1/2}} \qquad (2)$$

(e.g., Williams et al. 2000), with σ_v corrected for the effect of the thermal component as above. Figure 8 shows that, for virtually all clumps, $M > M_{\rm BE}$, implying that the effect of the pressure of the H II region is enough to make the clumps unstable to gravity. However, $M_{\rm BE}$ depends on the adopted line width of the clump: the $C^{18}O$ line width used here has the advantage that, being optically thin, it samples the velocity dispersion throughout the cloud. The ^{13}CO line width is systematically higher (see Table 3) by a factor of $\lesssim$2, which could lead to an underestimate of the Bonnor-Ebert mass by up to an order of magnitude.

Estimates of the masses of the clumps from $C^{18}O$ data are systematically higher than the continuum masses by up to an order of magnitude. The abundance of $C^{18}O$ may be lower than assumed, because of selective photodissociation or freezeout onto dust grains at low temperatures, but both of these effects would give an underestimate of the true gas mass. The $C^{18}O$ measurements were based simply on spectra taken toward the clump positions, without any attempt to remove a spatial background, as was done by Gaussian fitting in the continuum maps, leading to an overestimate of the clump mass, although this is unlikely to be more than a factor of 2.

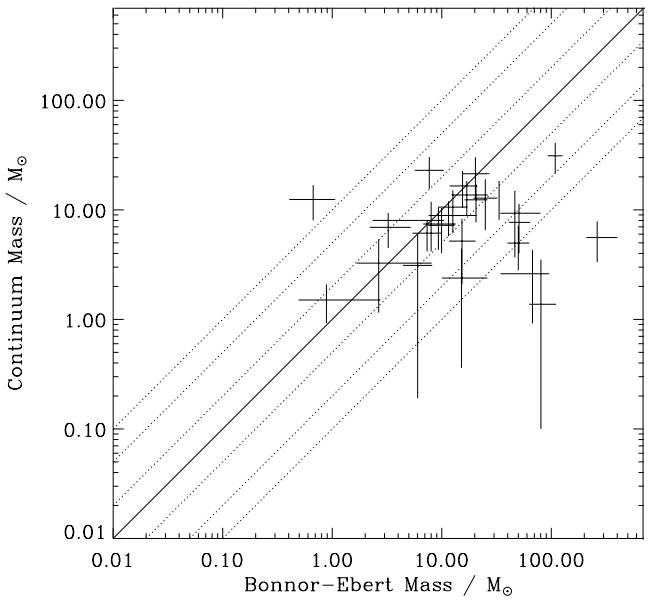

FIG. 8.—Estimated clump masses (from continuum data) compared to Bonnor-Ebert masses. The solid lines mark the locus of equal masses, and the broken lines mark loci where they differ by factors of 2, 5, and 10.

Inaccuracies in the continuum estimates may come from the assumed opacity, temperature, and gas-to-dust ratio. The assumed opacity is 2.5 times higher than the standard value of Hildebrand (1983), so the clump mass could be underestimated by a factor of $\sim$2. Furthermore, the dust temperature was taken to be equal to the gas temperature deduced from CO measurements. If the gas and dust are not well coupled, the dust could be significantly cooler: assuming a dust temperature of 30 K, when it is in fact 20 K, would result in a mass underestimate of a factor of 2 at 450 μm. The assumed gas-to-dust ratio may also be incorrect; this is known only to about a factor of 2 (Hildebrand 1983).

4.3.3. *Timescales and Evolution*

The evolution of the clumps may include three processes: the compression of the molecular gas by the shock front, the photoevaporation of the shocked gas by the ionization front, and the gravitational collapse of the gas to form new stars. The latter two processes are competitive: if the gas is dispersed by the ionization front before it can collapse, no stars will be formed. The future of the clumps therefore depends on the relative timescales of these processes.

The shock-crossing time ($\tau_{\rm shock}$) was evaluated using the results of Bertoldi (1989) and Bertoldi & McKee (1990), shown in Figure 9. The error bars take into account estimated errors in the physical quantities (mass and number density of the clump, distance from the ionizing stars). The most likely systematic error (not included in the error bars) arises from the dependence on electron temperature ($\propto T_e^{-0.9}$), which could increase the timescale by almost a factor of 2. The characteristic timescale for gravitational collapse is given by the free-fall time. More realistic studies of collapse (e.g., Larson 1969; Shu 1977) show that collapse takes longer than $\tau_{\rm ff}$, but still occurs within $\sim 2\tau_{\rm ff}$. The timescale over which the clump is destroyed by photoevaporation is given by $\tau_{\rm evap} = M/(dM/dt)$, where the rate of mass loss dM/dt is given by the mass flux through the IF, integrated over the whole clump (Bertoldi & McKee 1990); $\tau_{\rm evap}$ has the same electron temperature dependence as $\tau_{\rm shock}$.

These timescales are plotted for the clump sample in Figure 9. In general, $\tau_{\rm ff} > \tau_{\rm shock} > \tau_{\rm evap}$, suggesting that evaporation will be the dominant process. However, this does not take into account the effect of the external pressure on gravitational collapse. The continuum masses are larger than the Bonnor-Ebert mass for almost all clumps, so the gravitational collapse timescale is shorter than the sound-crossing time inside the clump. The shock-crossing time will be about an order of magnitude shorter than the sound-crossing time (since the shock velocity is comparable to the sound speed in the ionized medium). Since the free-fall timescale depends on the density, the collapse timescale will be altered by the

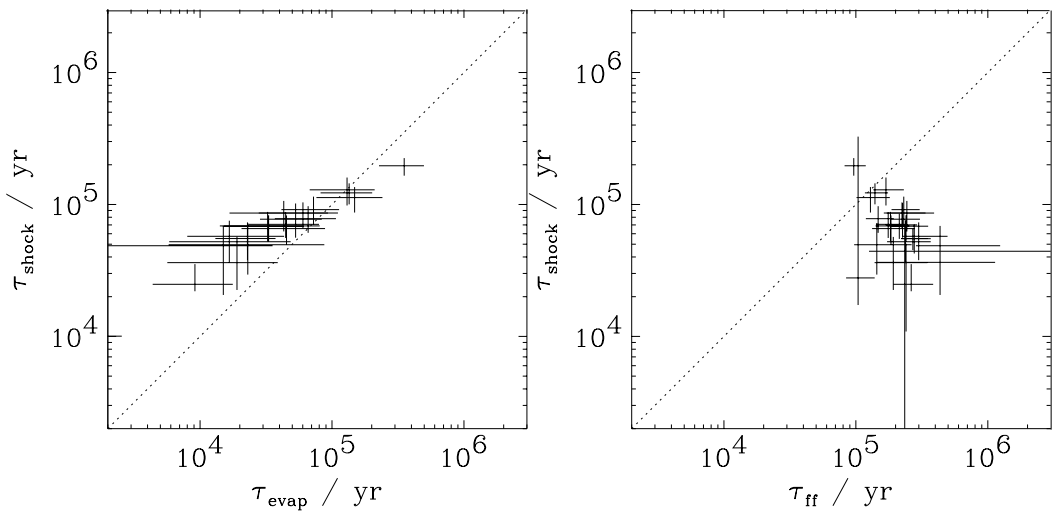

FIG. 9.—Estimated timescales for the clump sample. The broken lines mark loci where the timescales are equal. Both plots are calculated using the continuum masses of the clumps.

progress of the shock through the clump. If the estimates of the clump conditions reflect the unshocked gas, then the free-fall time will be rather shorter in the shocked gas and collapse more likely. It is unclear whether or not this effect will be sufficient, along with the effect of external pressure, to induce star formation before the clumps are photoevaporated. If the clump masses are significantly higher than estimated from continuum emission (as the $C^{18}O$ masses are), then the estimated timescales all become quite similar. In this case, given the likely increases in shock-crossing and evaporation times due to electron temperature effects and the effects of external pressure, it is quite likely that the clumps will collapse to form stars.

In summary, it appears that the molecular clumps around the H II region have not yet undergone implosion, and most of the material in the clumps is at low pressure—i.e., upstream of the shock front. By comparison, the "fingers" in the Eagle Nebula, M16 (White et al. 1999) appear to be close to pressure equilibrium, suggesting that they may have already undergone compression. The M16 fingers appear to extend further out into the H II region than their counterparts in M8, suggesting that they are somewhat older.

A serious limit on the accuracy of these prognostications is the fact that the UV flux incident on the clumps is estimated very roughly. It would be preferable to derive the physical characteristics of the ionized gas at the interface directly from radio continuum and optical emission-line data. A further concern is the large discrepancy between the clump masses traced by $C^{18}O$ and dust. It may be useful to take account of the gas density, as well as its temperature, to estimate the dust temperature, using models of gas/dust coupling. Once the physical conditions are better known, it should be possible to model the evolution of the clumps with more certainty and to assess whether or not a further generation of stars will form around the Lagoon Nebula.

5. CONCLUSIONS

The object of this paper is to characterize the clumpy structure of M8 and to relate it to the evolution of the region, using continuum maps at 450 μm, 850 μm, and 1.3 mm wavelengths. The consistency between wave bands is not very good: many detected clumps were rejected because the fitted positions did not agree, and the fitted areas have a large scatter—an effect that feeds directly through to the measured fluxes. Given the calibration stability of current bolometer receivers, these discrepancies pose a greater problem for the interpretation of submillimeter continuum data than the absolute flux calibration. The presence of the telescope error beam may be an important factor in these inconsistencies, together with the contamination of the dust continuum flux by other emission mechanisms. This is likely to be a particular problem with line emission (especially ^{12}CO) and contamination from PDRs, which have different spatial structure to the clump dust emission. There are possible solutions to these problems: in theory, the error beam can be dealt with by deconvolution; radio continuum imaging should allow free-free contamination to be removed; the effects of spectral line contamination may be removed by mapping the field and then subtracting the line emission directly. In order to account adequately for all the spectral lines in the passband, more spectral surveys are needed, concentrating on less chemically rich regions like M8. There is a large systematic discrepancy between estimated masses from $C^{18}O$ spectra and the estimated masses from continuum emission, which underscores the need for better knowledge of the properties of interstellar dust (particularly the opacity), and of the coupling of gas and dust, so as to have fairly accurate estimates of the dust temperature.

Nonetheless, these weaknesses do not cripple the study of the mass function, since they are mainly systematic. Kolmogorov-Smirnov statistics were used to fit a power law to the high-mass end of the clump mass distribution with index $\alpha = 1.7 \pm 0.6$, which agrees with the results of spectral-line studies of clump mass spectra on similar spatial scales. This in turn adds weight to the high-resolution continuum studies of nearby star-forming regions that find larger exponents ($\alpha > 2$) and a break in the mass spectrum (Motte et al. 1998; Testi & Sargent 1998), in contrast to the ^{12}CO study of Heithausen et al. (1998), which finds one power-law spectrum continuing over a very large range of scales. There is clearly more work to be done in understanding the mass spectrum of the interstellar medium; better completeness estimates would be particularly helpful.

It seems that the M8 clumps are still largely unaffected by the shocks driven into them by ionization fronts. Their future is not entirely clear, particularly because of the uncertainty in their mass. Although they seem incapable of spontaneous gravitational collapse, the effects of shock compression and external pressure from the ionized gas may be enough to induce star formation. By looking for chemical diagnostics of shocked and unshocked gas, it might be possible to assess the progress of the shock front through the clumps. Radio and optical data could be used to characterize the ionized layer at the interface between the clumps and the H II, to give improved estimates of the pressure balance. Together with improved estimates of the mass and density of the clumps, it should then be possible to predict their evolution with more certainty.

The James Clerk Maxwell Telescope is operated by the Joint Astronomy Center on behalf of the Particle Physics and Astronomy Research Council (PPARC) of the United Kingdom, the Netherlands Organisation for Scientific Research, and the National Research Council of Canada. This work is based in part on measurements made with the Heinrich Hertz Telescope, which is operated by the Submillimeter Telescope Observatory on behalf of Steward Observatory and the Max-Planck-Institut für Radioastronomie. N. F. H. T. gratefully acknowledges the receipt of a Research Studentship from PPARC. We wish to thank the anonymous referee for a thorough and patient reading of the original manuscript and for the suggestions that have improved it.

APPENDIX

GAUSSIAN FITTING

The fitted parameters for each elliptical Gaussian profile were the position of the Gaussian center, the amplitude, the FWHM of the major axis, the ellipticity, the position angle of the major axis, and the background value. A starting set of parameters is required by the fitting routine. Each clump was identified by eye, and the starting estimates of Gaussian parameters were as follows: position and amplitude were given by the map coordinates and value of the peak pixel; the major axis was taken to have the same FWHM as the beam; and the ellipticity, position angle, and background level were all set to very low values and allowed to vary. The starting model for the clumps was therefore a point source with flux equal to the peak intensity in the map on a zero background. The fitted Gaussian was subtracted from the map to give a residual map, which was used to fit the next source. This iterative scheme allows relatively faint clumps close to bright sources to be fitted. The fitting routine estimates the error in the fitted parameters by resampling the χ^2 hypersurface using a Monte Carlo method and determining the curvature. The fitted parameters tended to vary with the size of the box used to fit the Gaussian. The fitting was carried out with a number of box sizes, the residual images were examined by eye, and the best fit selected. If there was no significant difference between the residuals, the fit with the smallest FWHM was selected, on the assumption that the error beam would tend to bias the fitting toward unrealistically large Gaussians.

There are other possible approaches: a more sophisticated approach might involve fitting a form of power law to the brightness distribution, or even a model with power-law temperature and density profiles, which could fully take account of Rayleigh-Jeans failure, the coupling between density and temperature, etc. However, these techniques still require assumptions to be made about the source structure and the source profiles must be convolved with the beam structure in order to be fitted (e.g., Shirley et al. 2000)—by contrast, Gaussian fitting is much more straightforward.

In order to be accepted as having detections at both 450 and 850 μm, the positional offset between the fitted Gaussians was required to be less than 8″ (half a beamwidth). Then both the Gaussians were cross-referenced with the 1.3 mm map: if a 1.3 mm detection was within 15″ of both short-wavelength detections and within 8″ of at least one of them, the clump was accepted as having been detected at all three wavelengths. It seems likely that confusion or bad fitting plays a role in the lack of cross-referenced detections, along with the effect of noise in the map.

REFERENCES

Adams, F. C. 1991, ApJ, 382, 544
Bergin, E. A., Langer, W. D., & Goldsmith, P. F. 1995, ApJ, 441, 222
Bertoldi, F. 1989, ApJ, 346, 735
Bertoldi, F., & McKee, C. F. 1990, ApJ, 354, 529
Blake, G. A., Sutton, E. C., Masson, C. R., & Phillips, T. G. 1986, ApJS, 60, 357
Blitz, L. 1993, in Protostars and Planets III, ed. E. H. Levy & J. I. Lunine (Tucson: Univ. Arizona Press), 125
Bohuski, T. J. 1973, ApJ, 184, 93
Broguière, D., Neri, R., & Sievers, A. 1998, NIC Bolometer Users Guide Version 1.4-03 (IRAM)
Carr, J. S. 1987, ApJ, 323, 170
Draine, B. T., & Lee, H. M. 1984, ApJ, 285, 89
Dufour, R. J. 1994, Rev. Mexicana Astron. Astrofis., 29, 88
Elliot, K. H., Goudis, C., Hippelein, H., & Meaburn, J. 1984, A&A, 138, 451
Elmegreen, B. G. 1999, ApJ, 515, 323
Elmegreen, B. G., Efremov, Y. N., Pudritz, R. E., & Zinnecker, H. 2000, in Protostars and Planets IV, ed. V. Mannings, A. P. Boss, & S. S. Russell (Tucson: Univ. Arizona Press), 179
Emerson, D. T., Klein, U., & Haslam, C. G. T. 1979, A&A, 76, 92
Emerson, D. T. 1995, in ASP Conf. Ser. 75, Multi-feed Systems for Radio Telescopes, ed. D. T. Emerson & J. M. Payne (San Francisco: ASP), 309
Georgelin, Y. P., & Georgelin, Y. M. 1970a, A&A, 6, 349
Goldsmith, P. F., Bergin, E. A., & Lis, D. C. 1997, in IAU Symp. 170, CO: 25 Years of Millimetre-Wave Spectroscopy, ed. W. B. Latter et al. (Dordrecht: Kluwer), 113
Greaves, J. S., & White, G. J. 1991, A&AS, 91, 237
Greve, A., Neri, R., & Sievers, A. 1998, A&AS, 132, 413
Harvey, P. M., Thronson, H. A., Jr., & Gatley, I. 1980, ApJ, 235, 894
Heithausen, A., Bensch, F., Stutzki, J., Falgarone, E., & Panis, J. F. 1998, A&A, 331, L65
Helmich, F. P., & van Dishoeck, E. F. 1997, A&AS, 124, 205
Hildebrand, R. H. 1983, QJRAS, 24, 267
Hobson, M. P., Padman, R., Scott, P. F., Prestage, R. M., & Ward-Thompson, D. 1993, MNRAS, 264, 1025
Holland, W. S., et al. 1999, MNRAS, 303, 659
Hollenbach, D. J., Takahashi, T., & Tielens, A. G. G. M. 1991, ApJ, 377, 192
Humphreys, R. M. 1978, ApJS, 38, 309
Jenness, T., & Lightfoot, J. F. 1997, SURF User's Manual, SUN/216.1 (Starlink)
Johnstone, D., Wilson, C. D., Moriarty-Schieven, G., Joncas, G., Smith, G., & Fich, M. 2000, ApJ, 545, 327
Kreysa, E., et al. 1998, Proc. SPIE, 3357, 319
Krügel, E., & Siebenmorgen, R. 1994, A&A, 288, 929
Kurucz, R. L. 1979, ApJS, 40, 1
Lada, C. J., Gull, T. R., Gottlieb, C. A., & Gottlieb, E. W. 1976, ApJ, 203, 159
Lada, E. A., Bally, J., & Stark, A. A. 1991, ApJ, 368, 432
Ladd, E. F., et al. 1991, ApJ, 382, 555
Larson, R. B. 1969, MNRAS, 145, 271
Langer, W. D., & Penzias, A. A. 1990, ApJ, 357, 477
Lightfoot, J. F., et al. 1984, MNRAS, 208, 197
Loren, R. B. 1989, ApJ, 306, 142
Lynds, B. T., & O'Neil, E. J., Jr. 1982, ApJ, 263, 130
McKee, C. F., & Zweibel, E. G. 1995, ApJ, 440, 686
Melnik, A. M., & Efremov, Y. N. 1995, AZh Pis'ma, 21, 13
Messier, C. 1781, in Connoissance des Temps Almanac for 1784 (Paris), 217
Mitchell, G. F., Johnstone, D., Moriarty-Schieven, G., Fich, M., & Tothill, N. F. H. 2001, ApJ, 556, 215
Motte, F., & André, P. 2001, A&A, 365, 440
Motte, F., André, P., & Neri, R. 1998, A&A, 336, 150
Motte, F., André, P., Ward-Thompson, D., & Bontemps, S. 2001, A&A, 372, L41
Myers, P. C., Linke, R. A., & Benson, P. J. 1983, ApJ, 264, 517
Myers, P. C., & Goodman, A. A. 1988, ApJ, 326, L27
Nozawa, S., Mizuno, A., Teshima, Y., Ogawa, H., & Fukui, Y. 1991, ApJS, 77, 647
Oldham, P. G., Griffin, M. J., Richardson, K. J., & Sandell, G. 1994, A&A, 284, 559
Ossenkopf, V., & Henning, T. 1994, A&A, 291, 943
Panagia, N. 1973, AJ, 78, 929
Press, W. H., Flannery, B. P., Teukolsky, S. A., & Vetterling, W. T. 1986, Numerical Recipes (Cambridge: Cambridge Univ. Press)
Richer, J. S. 1992, MNRAS, 254, 165
Ristorcelli, I., et al. 1996, in The Role of Dust in the Formation of Stars, ed. H. U. Kaüfl & R. Siebenmorgen (Berlin: Springer), 121
Schilke, P., Groesbeck, T. D., Blake, G. A., & Phillips, T. G. 1997, ApJS, 108, 301
Serabyn, E., & Weisstein, E. W. 1995, ApJ, 451, 238
Shirley, Y. L., Evans, N. J., II, Rawlings, J. M. C., & Gregersen, E. M. 2000, ApJS, 131, 249
Shu, F. H. 1977, ApJ, 214, 488
Soifer, B. T., Pipher, J. L., & Houck, J. R. 1972, ApJ, 177, 315
Sptizer, L., Jr. 1978, Physical Processes in the Interstellar Medium (New York: Wiley)
Stutzki, J., & Güsten, R. 1990, ApJ, 356, 513
Sutton, E. C., Blake, G. A., Masson, C. R., & Phillips, T. G. 1984, ApJ, 283, L41
———. 1985, ApJS, 58, 341
Sutton, E. C., Jaminet, P. A., Danchi, W. C., & Blake, G. A. 1991, ApJS, 77, 255

Sutton, E. C., Peng, R., Danchi, W. C., Jaminet, P. A., Sandell, G., & Russell, A. P. G. 1995, ApJS, 97, 455
Testi, L., & Sargent, A. I. 1998, ApJ, 508, L91
Tothill, N. F. H. 1999, Ph.D. thesis, Univ. London
van Altena, W. F., & Jones, B. F. 1972, A&A, 20, 425
van den Ancker, M. E., Thé, P. S., Feinstein, A., Vázquez, R. A., de Winter, D., & Pérez. M. R. 1997, A&AS, 123, 63
Wall, W. F., et al. 1996, ApJ, 456, 566
Ward-Thompson, D., Motte, F., & André, P. 1999, MNRAS, 305, 143
White, G. J., et al. 1999, A&A, 342, 233
Williams, J. P., & Blitz, L. 1993, ApJ, 405, L75
Williams, J. P., Blitz, L., & McKee, C. F. 2000, in Protostars and Planets IV, ed. V. Mannings, A. P. Boss, & S. S. Russell (Tucson: Univ. Arizona Press), 97
Williams, J. P., Blitz, L., & Stark, A. A. 1995, ApJ, 451, 252
Williams, J. P., de Geus, E. J., & Blitz, L. 1994, ApJ, 428, 693
Woodward, C. E., et al. 1986, AJ, 91, 870
Zinner, E. 1996, in ASP Conf. Ser. 99, Cosmic Abundances, ed. S. S. Holt & G. Sonneborn (San Francisco: ASP), 147